

The Impact of the Discreteness of Low-Fluence Ion Beam Processing on the Spatial Architecture of GaN Nanostructures Fabricated by Surface Charge Lithography¹

I. M. Tiginyanu^a, O. Volciuc^b, M. A. Stevens-Kalceff^c, V. Popa^d, J. Gutowski^b,
S. Wille^e, R. Adelung^e, and H. Föll^e

^a*Institute of Electronic Engineering and Nanotechnologies, Academy of Sciences of Moldova, Academiei str., 3/3, Chisinau 2028, Moldova*

^b*Institute of Solid State Physics, University of Bremen, Bremen 28334, Germany*

^c*School of Physics, University of New South Wales, Sydney NSW 2052*

^d*National Center for Materials Study and Testing, Technical University of Moldova, 168, Stefan cel Mare Blvd., Chisinau 2004, Moldova*

^e*Institute for Materials Science-Functional Materials, University of Kiel, Kiel 24143, Germany*

e-mail: popa_sl@yahoo.com

Received November 17, 2012

Abstract—We show that the discrete nature of ion beam processing used as a component in the approach of surface charge lithography leads to spatial modulation of the edges of the GaN nanostructures such as nanobelts and nanoporated membranes. According to the performed Monte Carlo simulations, the modulation of the nanostructure edges is caused by the stochastic spatial distribution of the radiation defects generated by the impacting ions and related recoils. The obtained results pave the way for direct visualization of the networks of radiation defects induced by individual ions impacting a solid-state material.

DOI: 10.3103/S1068375513010146

Gallium nitride is a wide-band-gap semiconductor compound ($E_g = 3.4$ eV at 300 K) widely used in optoelectronics for the production of UV LEDs and lasers. The compound is promising for applications in high-power/high-temperature electronics and many investigations have been carried out in this regard. Note that the material exhibits pronounced radiation hardness that can be considerably strengthened by nanostructuring [1]. Recently [2, 3] we reported the fabrication of suspended GaN membranes with the thicknesses down to 1 nm by using a modified version of the so-called Surface Charge Lithography (SCL) developed by us previously [4, 5]. SCL is based on direct ion-beam-writing of surface negative charge with subsequent photoelectrochemical (PEC) etching of the GaN sample [3–5]. In this Letter, we show for the first time that the discreteness of ion beam processing used as a component of SCL has a considerable impact on the spatial nanoarchitecture of narrow or nanoporated GaN membranes, in particular it modulates the edges of the nanostructures which reflects the spatial distribution of the radiation defects generated by the impacting ions and related recoils.

The wurtzite *n*-GaN layers were grown by low pressure MOCVD on (0001) *c*-plane sapphire substrates.

A buffer layer of 25 nm thick GaN was first grown at 510°C. Subsequently a 3 μm thick *n*-GaN layer was grown at 1100°C. The concentration of free electrons was of the order of 10^{17} cm⁻³, while the density of threading dislocations was in the range of $(10^9–10^{10})$ cm⁻². Arrays of parallel lines 10 nm in width were directly written on the sample surface by 30 keV Ga⁺ ions provided by a focused-ion beam (FIB) system with a fluence of approx. 3×10^{12} cm⁻². At the same time selected areas of the sample surface were treated in automated patterning mode by the focused ion beam resulting in gentle ion-beam-processing of circular-like areas constituting a periodic network of ion-implanted negatively charged surface regions and merging with each other at the edges. The dose of the ions in the treated areas was lower than in the previous case. According to the concept of SCL [2–5], processing of the sample surface by low-energy ions creates deep acceptors that trap electrons and form a shield of negative charge that protects the material against PEC dissolution. Monte Carlo simulations predict the main projected range of 30 keV Ga⁺ ions in an amorphous GaN matrix to be about 14 nm [5]. In crystalline GaN the range may be enhanced due to ion-channelling effects. PEC etching was carried out at 300 K in a stirred 0.1 mol aqueous solution of KOH for periods up to 1.5 h under in-situ UV illumination provided by

¹ The article is published in the original.

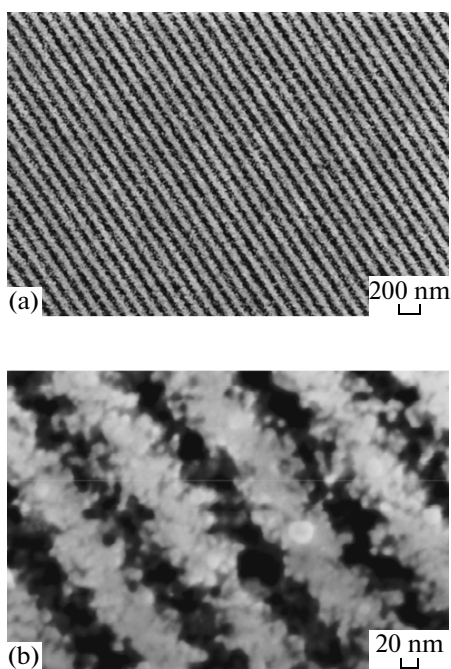


Fig. 1. SEM images taken at different magnifications from arrays of GaN nanobelts.

focusing the radiation of a 350 W Hg lamp to a spot of 5 mm in diameter on the sample surface. The sample morphology was studied using a Zeiss ultra plus scanning electron microscopes (SEM).

A JEOL 7001F field emission SEM equipped with a Gatan XiCLone cathodoluminescence (CL) microanalysis system was used for comparative morphological and CL characterization. The monochromatic microcathodoluminescence (μ -CL) images were collected using a Peltier cooled Hamamatsu R943-02 photomultiplier tube.

Figures 1a and 1b are SEM images illustrating an array of GaN “nanobelts” fabricated by employing SCL. Interestingly, the nanobelts exhibit many protrusions along the edges. To throw light upon this phenomenon, one should take into account the discrete nature of the ion beam processing applied. This feature will be discussed below.

Figure 2a illustrates the morphology of the GaN surface area treated by FIB in automated patterning mode with subsequent PEC etching. Exploration by SEM revealed the formation of an ultrathin membrane with ordered nanopores that is supported on a network of whiskers representing threading dislocations [6]. The membrane is nanoporated as a result of bridging between neighbouring circular-like areas patterned by FIB. Figures 2b,c,d show monochromatic and color composite cathodoluminescence images taken from the same portion of the membrane. Characteristic GaN CL is observed. As expected, the ultra-thin membrane exhibits mainly very low intensity yellow luminescence at ~ 2.25 eV [6], while the

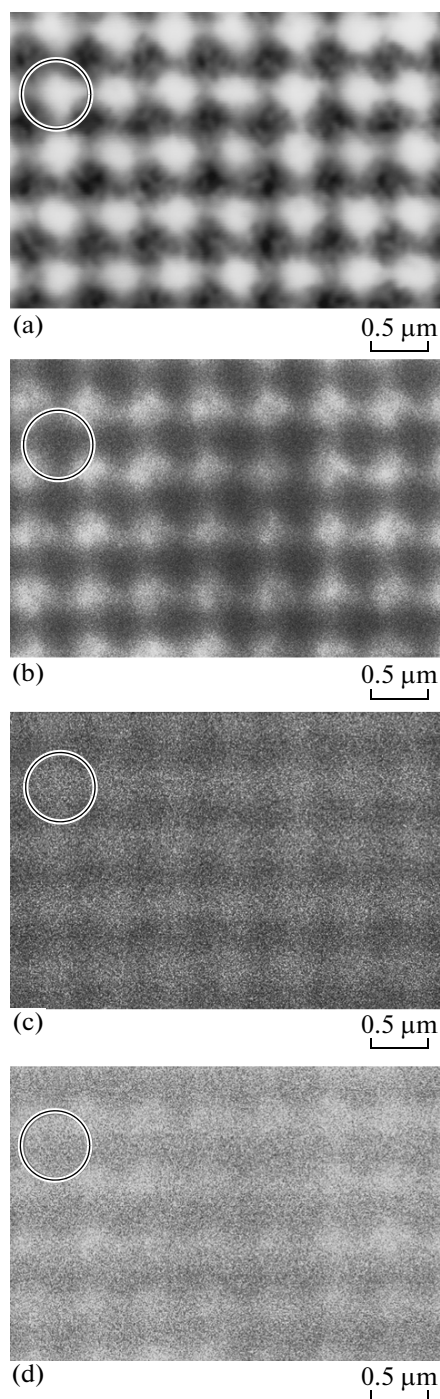


Fig. 2. SEM image taken from a portion of the nanoporated GaN membrane (a), and comparison of monochromatic ((b) 3.4 eV; (c) 2.25 eV) μ -CL images with two-color (blue—3.4 eV; yellow—2.25 eV) composite image (d). The red circles mark the same position in the GaN membrane.

more intense UV luminescence at ~ 3.4 eV comes from the underlying regions of PEC-etched GaN. An interesting feature is the irregular nature of the shape of the membrane holes, see Fig. 2a.

Optimization of the Composition, Structure, and Properties of Electrode Materials and Electrospark Coatings for Strengthening and Reconditioning of Metal Surfaces

A. V. Paustovskii, Yu. G. Tkachenko, R. A. Alfintseva, S. N. Kirilenko, and D. Z. Yurchenko

*I.N. Frantsevich Institute for Problems of Materials Science, National Academy of Sciences of Ukraine,
ul. Krzhizhanovskogo 3, Kiev, 03680 Ukraine*

e-mail: tkachenko_yuri@ukr.net

Received January 24, 2012

Abstract—The structure and phase composition of Ni–Cr–Al alloys doped with Si, Ti, Mn, and Co have been studied. An eutectic three-phase structure was found to be in the doped alloys. Doping with Si and Ti increases the microhardness and wear resistance of the alloys. The highest coefficient of the mass transfer (0.75) during the electrospark alloying is observed for Co-containing alloys. The coatings with the doped alloys have a higher wear resistance than those with the Ni–Cr–Al basic alloy. Steel 45's heat resistance is increased after the electrospark doping with Si-, Ti-, Mn-, and Co-containing alloys by 4, 4.3, 5.1, and 4.6 times, respectively. The electrode materials have been developed for the electrospark reconditioning of workpieces based on PE8418 (Ni–Ni₃B–Cu–Si) with the additions of titanium carbide, chromium carbide, and tungsten carbide, which make it possible to manufacture coatings up to 5-mm thick. The results of the investigation of the erosion properties of B₄C–TiB₂ alloys manufactured using the method of reactive sintering under hot pressing of B₄C–TiO₂ powder blends that were used as the electrode materials for the electrospark hardening of titanium surfaces are presented. The tests show that, in the surface layers of the electrode materials, under the impact of the electric discharge, the boron carbide content substantially decreased, while the quantity of titanium borides increased and new phases of TiC_xN_y, TiO₂, and Ti appeared. Only these components are transferred onto the surface of the titanium alloy and form there a protective coating up to 100 μm thick with high hardness (32–43 GPa) and wear resistance. The materials developed are promising for their application as the electrodes in the electrospark alloying of construction steels and titanium alloys.

DOI: 10.3103/S1068375513010109

INTRODUCTION

The previous works [1] and practical experience showed that the technology of manufacturing and the composition of the electrodes make it possible to optimize the erosion properties of electrode materials, which are required for depositing wear- and heat-resistant electrospark coatings of necessary thicknesses.

In this work, using the analysis of the printed data for the further improvement of Ni–Cr–Al based alloys, the elements for their doping were determined. Silicon [2] is considered to be the most efficient doping component, which increases the heat resistance of Ni–Cr–Al alloys. Its application in the composition of the coatings from Ni–Cr and Ni–Cr–Al [3] is becoming more extensive. Small amounts of silicon can be dissolved in an intermetallic compound NiAl, thus enhancing its hardness and heat resistance [4].

The test results [5] show that deposition of titanium on Ni–Cr–Al alloys that contain (40–50) wt % of chromium leads to the formation of cinder Cr₂O₃ and to an increase in the adhesion in the alloys.

The study of the heat resistance of the chromium-based alloys [6] showed that doping with manganese allows a more uniform layer of cinder Cr₂O₃ to be obtained.

The Ni–Cr–Al alloys with an eutectic structure doped with cobalt are shown to have an advantage in heat resistance [7] compared to the alloys with a close composition but without an eutectic structure.

Recently, the composites based on nonmetallic heat-resistant compounds such as boron carbon [8] and aluminum nitride [9, 10] have been found to be used as the electrode materials more extensively. However, the extensive application of boron carbon in practice is limited by its brittleness. The use of a second structural component (a metal additive or a less brittle and hard component such as the heat-resistant compound TiB₂) in the materials based on boron carbide is known to substantially eliminate this problem.

In the scope of the aforementioned, the aims of this work are to improve the composition and to optimize the technology of manufacturing of electrode materials based on Ni–Cr–Al alloys due to the introduction of doping elements (Si, Ti, Mn, and Co) into them; to

develop electrode materials for the electrospark reconditioning of workpieces based on the alloy PE8418 (Ni–Ni₃B–Cu–Si) and carbides of titanium, chromium, and tungsten; and to develop electrode materials of the B₄C–TiB₂ system for strengthening metal surfaces.

COATINGS FROM Ni–Cr–Al ALLOYS DOPED WITH Si, Ti, Mn, AND Co

The investigations [1] of the properties of the electrospark coatings from Ni–Cr–Al alloys showed that the wear resistance and heat resistance are increased more efficiently using Ni–Cr–Al alloys whose phase composition is in the range of a ternary eutectic that consists of α , γ , and β solid solutions based on chromium, nickel, and intermetallic NiAl. Those coatings increase the wear resistance of the constructional steel by 2–2.5 times, the heat resistance by 5–7 times, and the coefficient of the mass transfer under the ESA reaches 80%. The optimal content of the components in this alloy is as follows: Ni is (50–50.5); Cr is (40–41); Al is (9–9.5) wt %. Hereafter, this alloy will be referred to as 4A.

For the purpose of the development of the electrode materials, the structure and phase composition of the Ni–Cr–Al alloys of the electrospark coatings doped with Si, Ti, Mn, and Co have been studied. The chemical composition of the alloys developed is listed in Table 1.

Nickel electrolytic H-O; chromium refined EPX-0 with 99.9% purity; highly purified aluminum 9-995; and Si, Ti, Mn, and Co with 99.9% purity were used for the smelting. The latter was performed (using 1-kg ingots from the above alloys for the electrodes) in an electric resistance furnace in an inert atmosphere in alundum melting pots followed by casting in cylindrical 50-mm-long forms 6 and 12 mm in diameter.

In the nickel-based cast alloys, a plate-rod-like eutectic three-phase structure is observed, which consists of an α solid solution based on chromium, a γ solid solution based on nickel, and a β -phase solid solution based on intermetallic NiAl.

Doping of the 4A alloy with silicon, titanium, and manganese does not affect the eutectic character of the structures. Doping with cobalt nearly does not change the morphology of the eutectic that is registered in the 4A base alloy.

The X-ray phase analyses showed the presence of three phases based on solid solutions of nickel, chromium, and intermetallic NiAl in the basic 4A alloy.

The study of the microhardness under the load on the indenter of 1N of the cast alloys (Table 2) showed that the doping with silicon and titanium of the basic alloy increases the microhardness from 7.5 to 8.9 and 8.7 GPa, respectively. Admixtures of manganese decrease the microhardness to 6.2 GPa, and those of cobalt almost do not change it (7.4 GPa).

Table 1. The chemical composition of the doped alloys based on Ni–Cr–Al

Ordinal number	Alloy	Content of elements, wt %						
		Ni	Cr	Al	Si	Ti	Mn	Co
1	4A	50	41	9	–	–	–	–
2	4A Si	49	40	9	2	–	–	–
3	4A Ti	49	40	9	–	2	–	–
4	4A Mn	49	40	9	–	–	2	–
5	4A Co	48	38	9	–	–	–	4

Table 2. The values of the hardness and wear of the Ni–Cr–Al alloys doped with Si, Ti, Mn, and Co

Material	Hardness HRC	Microhardness, GPa	Friction characteristics	
			I , $\mu\text{m}/\text{km}$	f
St. 45	32	2.37	39.5	0.35
St.30XGSA	38	3.4	34.6	0.30
VT-22	21	3.2	70.4	0.40
Alloy 4A	60	7.5	14.7	0.32
Alloy 4A Si	64	8.9	12.1	0.30
Alloy 4A Ti	63	8.7	12.8	0.31
Alloy 4A Mn	58	6.2	16.4	0.34
Alloy 4A Co	59	7.4	14.8	0.32

The tests on the microhardness show the advantages of doping the eutectic alloys with silicon and titanium. It obviously results from the fact that silicon and titanium can be dissolved in intermetallic NiAl, thus enhancing its microhardness.

The tests on the friction and wear under dry sliding friction were carried out in the air at room temperature according to a shaft–plane scheme using an MT-68 friction machine [11, 12] at a sliding velocity of 10 m/s and a load of 5 kg. A 40-mm-diameter ring (shaft) from hardened steel 65G with a roughness of the working surface of $R_a = 0.2 \mu\text{m}$ was used as the counterbody. The 12-mm-diameter cylindrical specimens from the developed alloys or steel 45 and 30KhGSA with coatings on the flanks were tested. During the tests, the coefficient of the friction f and the intensity of the wear I ($\mu\text{m}/\text{km}$) were determined.

The direct dependence of the wear of the developed alloys on their hardness was defined during the tests. The wear of the alloys doped with silicon and titanium decreases to 12.1 and 12.8 $\mu\text{m}/\text{km}$. The wear of the A4 alloy doped with manganese increases to 16.4 $\mu\text{m}/\text{km}$.

The study of the kinetics of the mass transfer of the nickel-based alloys was performed using an EFI-46 facility in mode III; i.e., the frequency of the oscilla-

Dependence of the Yield of Carbon Nanomaterials on the Molecular Structure of Organic Liquids in the Process of Electrodischarge Treatment

N. I. Kuskova, S. V. Petrichenko, P. L. Tsolin, and V. Yu. Baklar'

*Institute of Pulse Processes and Technologies, National Academy of Sciences of Ukraine,
pr. Oktyabr'skii 43-A, Nikolaev, 54018 Ukraine*

e-mail: defr@iipr.com.ua, iipt@iipr.com.ua

Received February 27, 2012

Abstract—It was studied experimentally how the yield of the powder products in the process of continuous electrodischarge synthesis of carbon nanomaterials and the pyrolytic treatment of the concomitant gas mixtures depends on the structure and properties of the raw materials. Liquid organic substances—alcohols and acyclic and cyclic saturated hydrocarbons—were used as the raw materials.

DOI: 10.3103/S1068375513010067

INTRODUCTION

The electrodischarge treatment of organic liquids gives the possibility to induce extremal conditions in these liquids primarily related to their temperature and pressure. This leads to the destruction and decomposition of the molecules of the treated material with the subsequent formation of various carbon nanomaterials (CNM) with a complex of unique properties and gas mixtures of hydrogen and lower hydrocarbons [1–4].

The possibility of preparation of various kinds of CNM appears since organic liquids are used, which differ in the degree of hybridization of carbon atoms in the molecule and the structure of the molecule and also in the regime of the energy input. In comparison with various known methods of preparation of CNM (electric arc, CVD, detonation, etc.), the electric discharge method is characterized by the simple variation of the electric discharge parameters, which allows one to change the dynamic synthesis conditions in a wide range; moreover, it is not necessary to create special conditions in the reactors (a vacuum, an inert gas atmosphere, etc.).

The process's control with the aim to increase the yield of the product, which contains primarily one kind of CNM, and increasing of the efficiency of the material's treatment are urgent problems for the development of the electric discharge technology of CNM synthesis. The solution of these problems is associated with the necessity to perform research and determine how the yield, phase composition, and structure parameters of the synthesized materials depend on the kind of the organic material chosen, on the energy input regimes, and the technological parameters of the treatment. The results of this

research can improve the development of our insights into the mechanisms of the electrodischarge synthesis.

The aim of this work is to study the yield of powder CNM in the process of the continuous electric discharge treatment of organic liquids and the pyrolysis of the generated gases as a function of the number of the carbon atoms in the molecules of organic liquids and their molecular structure.

RESEARCH METHOD

Liquid hydrocarbons, which refer to cyclic and acyclic saturated hydrocarbons, hydrocarbon mixtures, and alcohols, were chosen as the initial raw materials. In particular, pentane, cyclopentane, hexane, cyclohexane, ethanol, butanol, and TS-1 kerosene (a hydrocarbon mixture) were subjected to continuous electrodischarge treatment. This choice was made according to the following considerations. Cyclopentane and cyclohexane possess a similar molecular structure—they contain a ring. The carbon atoms in them are in the state of sp^3 hybridization, but the molecules of the liquids contain different numbers of carbon atoms. In each of the pairs cyclopentane–pentane and cyclohexane–hexane, the molecules contain the same number of carbon atoms in the state of sp^3 hybridization, but their structure and the number of C–C and C–H bonds is different. The molecules of ethanol and butanol contain different numbers of carbon atoms and one oxygen atom; its role in the intermediate plasmachemical reactions is not clear.

The experiments were performed using an installation for the preparation of carbon nanostructures (Fig. 1) under the same conditions: the charge voltage

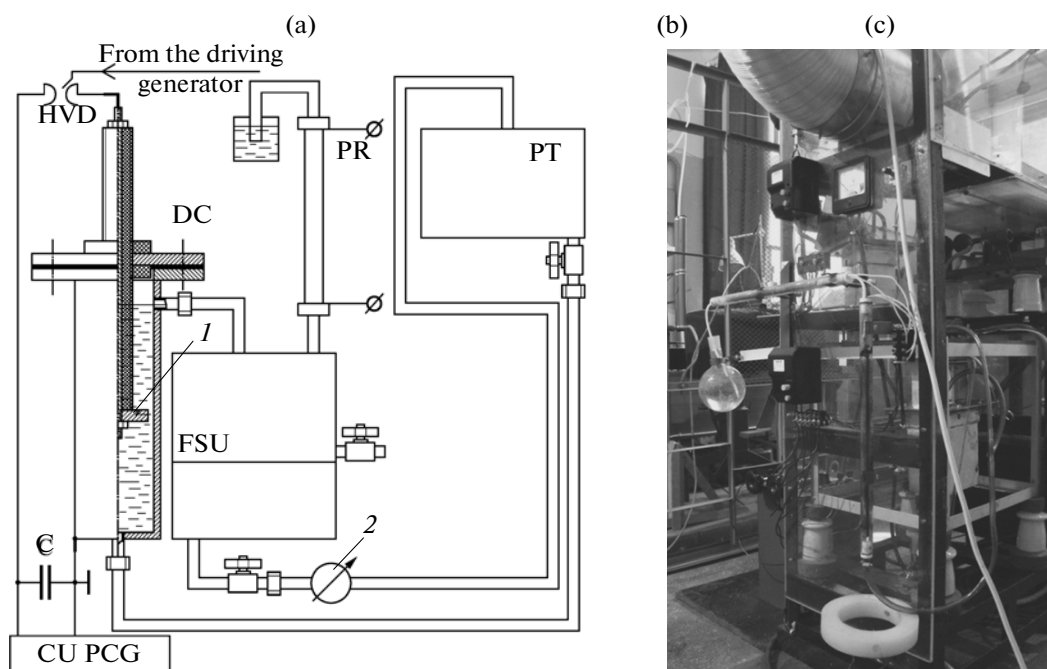


Fig. 1. Schematic view (a) and the photographs of the installation (b) and pyrolytic reactor (c).

of the capacitor battery U_0 , the capacitance of the energy storage (the capacitor battery) C , the volumetric speed of the liquid's circulation in the hydrosystem of the experimental installation v_{vol} , the repetition frequency of the charge pulses f , and the duration of the electrodischarge treatment $\tau = 3600$ s.

The width of the annular spacing between anode (1) and the wall of the cylindrical discharge chamber (DC) was the same for all the experiments. It was chosen taking into account its maximum value at which a stable electric discharge is formed in the named liquids at the specified parameters of the discharge loop. The repetition frequency of the discharge pulses was determined for the chosen volumetric speed of the liquid circulation performed by pump (2) for the specified thickness of disk anode (1). This ensured the dose of the electric discharge energy for the specified volume of the liquid during its flow from the pressure tank (PT) through the annular spacing in the reactor. The duration of the treatment allowed us to synthesize a CNM quantity sufficient for the studies.

To prepare CNM by virtue of pyrolysis of the gas mixtures formed during the electrodischarge treatment, the installation was equipped with a pyrolytic reactor (PR) with a heating element enclosed in a thermostable casing and a reservoir for collecting the CNM. Its upper part was connected with the lower part of the casing and its lower part with the gas output pipe with a filtration and separation unit (FSU) [5].

The construction of the installation makes it possible to vary the degree of heating of the gas mixtures from 700 to 1200 K; this allowed us to optimize the

process of their pyrolytic decomposition. The temperature was measured using a thermocouple of a Mastech MY64 multifunction instrument.

Under the action of the electrodischarge pulses on the hydrocarbons or in the process of their pyrolysis, the destruction of the molecules and the splitting of the hydrogen atoms occurred according to the following equation:



The carbon can be eliminated in the solid phase in various allotropic modifications.

With the aim to theoretically calculate the maximum mass of the nanocarbon m_{theor} , which can be obtained in the plasmachemical reaction according to Eq. (1) at the electrodischarge treatment of the raw material with its mass $m_{\text{r.m.}}$, we calculated the molar masses of the raw material $M_{\text{r.m.}} = 12n + k$ and the end product $M_{\text{pr}} = 12n$. Then,

$$m_{\text{theor}} = m_{\text{r.m.}} M_{\text{pr}} / M_{\text{r.m.}} = m_{\text{r.m.}} 12n / (12n + k). \quad (2)$$

The practical yield of the nanocarbon $\gamma = \gamma_1 + \gamma_2$ was calculated using the experimentally determined mass m_{pr}^1 and the yield γ_1 of the nanocarbon prepared as a result of the complete electrodischarge treatment of the organic liquid, and the mass m_{pr}^2 and the yield γ_2 of the nanocarbon prepared by the pyrolysis of the gas mixture if the carbon was eliminated, by the total mass of the raw materials without any residue:

$$\gamma_{1,2} = m_{\text{pr}}^{1,2} / m_{\text{theor}} = (1 + k/12n)(m_{\text{pr}}^{1,2} / m_{\text{r.m.}}). \quad (3)$$

Theoretical Grounds for the Calculation of the Electroconvective Heat and Mass Transfer

F. P. Grosu, M. K. Bologa, and Al. M. Bologa

Institute of Applied Physics, Academy of Sciences of Moldova, ul. Akademiei 5, Chisinau, MD 2028 Republic of Moldova

e-mail: mbologa@phys.asm.md

Received March 21, 2012

Abstract—A brief analysis of the state-of-the-art in the area of heat and mass transfer from the point of view of its intensification, as well as the design of heat exchangers based on the use of strongly nonuniform electric fields and the presence of a corona discharge, is presented. With an electric filter as an example, there are considered the peculiarities of the electroconvective heat and mass exchange based on the principle of corona discharges. The main problems that arise at the design of heat and mass transfer exchangers, such as how to determine the output characteristics—the temperature as a function of time in the case of heat transfer and the dispersed phase concentration in the case of mass transfer—are formulated. A working equation describing the above mentioned problems is obtained and the corresponding partial solutions are found.

DOI: 10.3103/S1068375513010055

INTRODUCTION

The calculation of the heat and mass transfer and the design of appropriate devices suggest not only the determination of the geometric characteristics but the physical ones as well, among which the time dependences of the liquid temperature $T(t)$ and/or the concentration $\varphi(t)$ of the dispersed particles in the case of mass transfer are of primary importance. These characteristics can be defined as those averaged by the heat and mass carrier volume except for the volume of the boundary layers (BL), where sharp changes of both temperature and concentration take place. Here, due to the rapid mixing of the medium with the convective heat and mass transfer, the averaged values will almost coincide with the output ones (see Fig. 1, “Outlet”). There automatically originates the problem of the steady (at $t \rightarrow \infty$) regime values. These and some other questions associated with the nonstationary transfer of heat and mass and concerned with the design of heat and mass exchangers and the operation of them are considered in this work.

The apparatus’s design reduces mostly to the analysis of the occurring processes complicated in our case due to the presence of the electric field used to enhance them. Thus, the processes are electroconvective; the working media should be dielectric (perfect or imperfect), thus permitting the presence of fields with sufficiently high intensity ($E \sim 1$ kV/cm and more). Such fields cause electrohydrodynamic (EHD) flows [1], also known as electroconvective ones [1, 2], thanks to which the transfer processes are substantially enhanced.

The specific nature of the enhancing effect of electric fields on the heat and mass transfer processes

(in particular, the heat exchange, its reasons, and regularities) are reflected in many works, among which are the papers on heat transfer by the discoverers of the effect [3–7], reviews [8, 9], monograph [10], as well as works [11–13]. The last one concerns a magnetic liquid (ML) but not the dielectric working media traditionally considered in electrohydrodynamics. This work can play the role of a connecting link between electrohydrodynamics and magnetohydrodynamics (MHD) from the point of view of the usage of the joint actions of electric and magnetic fields on media with various engineering and scientific aims. Really, a constant electric field is a substantial factor of the intensification of the magnetic fluid heat transfer [13], and the magnetic field has a magnetohydrodynamic effect on the ML. Consequently, there seemed no escaping

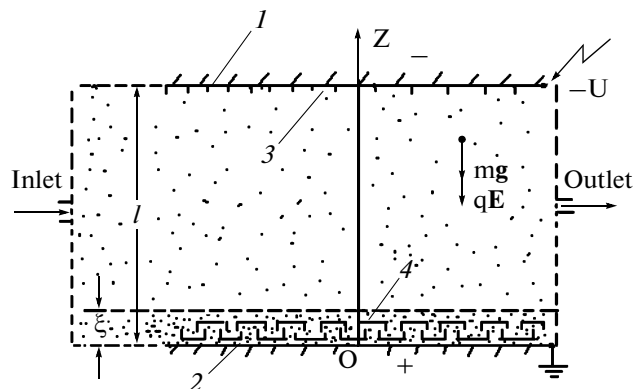


Fig. 1. The principal structure of an electrofilter.

the conclusion of a possible integrated and peculiar EMHD effect in the case of the simultaneous application of electric and magnetic fields on a magnetic liquid [14]. However, it will be in future, but here we consider the effect of an electric field on the heat exchange in an ML as one of the numerous examples specific to EHD processes.

Electric fields also have a significant effect on mass transfer, for instance, in the case of electric filtration [15], which is explained both by the electric charging of dispersed particles and the accompanying EHD phenomena. These questions and some others (in particular, concerning the complex heat and mass transfer in the case of an air–vapor mixture’s condensation in an electric field) remain the subject of our research [16]. One of the conclusions implies that the heat and mass transfer processes, though described by complicated equations, can be treated rather simply. This physicomathematical treatment can be accepted not only as a model in order to physically explain the phenomena and facts observed experimentally but also as the theoretical suppositions when designing heat and mass exchangers.

In the following, we need to know the design features of heat and mass exchangers; for this cause, let us consider a representative example of an electric filter [15]. A system of electrodes is used in it favoring the inception of a “corona” discharge as the main factor causing the observed phenomena. This factor has been selected because it is not only the most effective and easily realized but it is frequently used when EHD is concerned [17].

PECULIAR FEATURES OF AN ELECTRIC HEAT AND MASS EXCHANGER BASED ON THE “CORONA” DISCHARGE PHENOMENON

Traditionally, the electric field of a parallel-plate or cylindrical capacitor or some other system of electrodes is imposed on a heat and mass carrier. Obviously, the field effect on the heat and mass transfer is different; therefore, the selection of an electrode system is rather important in practice. Much experimental information on the heat transfer in an electric field with various geometric configurations can be found in the literature, in particular, in [10]. The analysis of it makes possible the conclusion that those electric heat and mass exchangers in which a “corona” discharge is used are the most efficient. One comes to similar deductions reading works on electric filtration [15]. The notion of a corona discharge (CD), which is inherent to gases, is used by the authors in the case of imperfect dielectric (low conducting) liquids; we restrict ourselves to considering only such liquids. Two factors serve as the basis to expand the notion of CD: its threshold and hydrodynamic aspects, which are generally analogous both for gases and liquids. Indeed, in both cases, a corona discharge is typical for sharply

nonuniform electric fields in the case of the electric voltage threshold (U_{cr}) and is attended by the strongly pronounced EHD phenomena known as the electric wind (EW) [18–20]. The physical meaning of these phenomena is that, in sharply nonuniform fields near active (pointed) electrodes, there are possible high field intensities \mathbf{E} sufficient for the existence of ionization not only in gases but in liquids as well. At this, the charge carriers opposite to the sign of the active electrode are neutralized on it or recharged. In both cases, this causes the generation of free spatial charges with the nonzero space density ($\rho \neq 0$) in a rather large area beyond the narrow “corona” layer immediately at the electrode’s surface; the interaction of the field with these charges in a dielectric liquid or gas results in the observed EHD phenomena (EW).

The physicomathematical explanation of the mentioned above in a classic approximation [18] is rather simple. In the general formula for conductivity, outside the corona layer, they restrict themselves only to a summand to which there correspond the charge carriers of the active electrode sign, which works out to the following formula for the current density at CD:

$$\mathbf{j} = k\rho\mathbf{E}. \quad (1)$$

Hence, in an EHD approximation—the “freezing in” of these charges into a liquid—there follows an equally simple and important formula for the driving force of the EHD phenomena:

$$\mathbf{f} = \rho\mathbf{E} = \mathbf{j}/k, \quad (2)$$

where k is the mobility of the carriers with the active electrode’s sign. This formula shows that it is the current through the system that is a determining characteristic of the EHD phenomena at a corona discharge. More accurate numerical calculations are presented in work [21]; however, the classical approximation works well in practice, as is evidenced by the numerous experimental data on heat transfer under corona discharge conditions [10].

Let us return to the design features of the electric heat and mass exchangers whose working principle is based on formulas (1) and (2). In most common cases (a cylindrical capacitor, employed, for instance, for the heat and mass transfer at the condensation of an air–vapor mixture in an electric field or a “plate–wire” electrode system used at the electric filtration (EF) of liquid dielectrics to produce strong fields), we used wires of comparatively large diameters (1.0–2.0 mm) but with the holed enamel insulation [22, 23]. When a high voltage is applied to the system, there arise great field intensities that are necessary and sufficient for the corona inception.

Simultaneously with the corona discharge from the holes, there appear some jet EHD flows “squirting”

Allowance for the Interaction between the Underwater Electric Discharge Channel Plasma and the Shock Wave Reflected from the Chamber's Wall

K. V. Dubovenko

Nikolaev State Agrarian University, ul. Parizhskoi Kommuny 9, Nikolaev, 54010 Ukraine

e-mail: dubovenko2010@gmail.com

Received February 2, 2012

Abstract—The numerical simulation of a spark discharge formed along the axis of a cylindrical chamber filled with water has been carried out in the magnetohydrodynamic approximation. The simulation results are compared with the data known from the literature. The analysis of the spatiotemporal distribution of the pressure and temperature in the discharge chamber has been performed with due account for the interaction between the shock waves excited by the spark discharge and reflected from the chamber's wall and the plasma channel.

DOI: 10.3103/S1068375513010031

INTRODUCTION

Due to the process conditions in pulse discharge devices for various applications, a discharge channel is usually formed in chambers of finite size. Some multi-electrode systems of high-voltage pulse discharge units are also used. If the shock wave generated by the discharge in the neighboring interelectrode gap or reflected from the chamber's wall manages to reach the channel during the release of the stored energy in the plasma, the problem to study the interaction between the high-current discharge plasma and the shock waves becomes practically important. The analysis of the research works carried out previously [1–6] shows that the time–space interaction between the plasma channel and the shock waves has not received proper attention.

A number of articles are dedicated to the examination of the characteristics of underwater electric discharges. The investigations whose results are presented in works [7–11] are devoted to the study of the radiation characteristics, the thermodynamic properties, and the water–plasma transfer coefficients. The central tenets of the theory of dense nonideal low-temperature plasma have been developed in works [12–16]. The dependences of the plasma's specific conductivity and pressure on the temperature and density (the particle concentration) with account for the plasma's nonideality have been determined [17].

The obtained data make up some source information to develop some calculation models in which the following basic assumptions have been initially accepted: the homogeneity of the radial distribution of the characteristics in the channel, and the incom-

pressibility of the liquid around the plasma channel [18]. The first assumption allows one not to consider the electrodynamic and thermal processes in the elementary volumes of the region occupied by the discharge plasma when describing the transition process in terms of the equation for the electric circuit with the discharge channel being its element with lumped parameters. The second assumption has helped to establish an approximation between the channel's expansion rate and the pressure with the unconsidered time–space processes beyond the current conducting area.

Later on, this approach was developed in a number of works in which there was established an interrelation between the pressure in the channel and the plasma's electric conduction being the channel section-averaged one [2]. These models, which adequately described a number of the integral characteristics of the discharge (the current, voltage, and radius), at that time did not allow one to calculate the hydrodynamic field within the discharge chamber's volume. The application area of them to estimate the pressure in the interelectrode gap was limited to discharges with small power when the channel's expansion rate is much less than the velocity of sound.

Because of these limitations, it becomes necessary to elaborate some models that include only one basic assumption (unlike the models considered above)—the homogeneity of the radial distribution of the characteristics in the discharge channel. In this case, the simultaneous solution of the discharge channel energy equation and the hydrodynamic equations allows one to avoid the second assumption and, thus, to describe

with sufficient accuracy the pressure field and the fluid's motion beyond the current-conducting area in the interelectrode gap. The models in which such an approach was realized were one-dimensional or two-dimensional [19–22]. Experimentally recorded relations of the discharge channel's expansion kinematics [20] or an empirically found universal law of the power input rate were initially used in them [21]. In [23], there is implemented a closed model that describes the hydrodynamic processes beyond the discharge channel at a two-dimensional approximation, and the energy input into the plasma has been calculated with regard for the equations of the electric discharge circuit. The considered models allowed us to obtain a number of analytic results that found important practical use in the sphere of electric discharge technology.

However, it should be noted that the field of application of the considered models is limited by a number of conditions. For instance, it is rather difficult to use them when the processes of the radiation heat transfer, the interaction between the channel plasma and the shock waves, and the discharges in small volumes are investigated. The results uniquely show that the characteristics of the plasma channel are nonuniformly distributed along its radius [19, 20, 24].

To solve such problems, it is reasonable to consider the whole area of the interelectrode gap, including the discharge channel, at the continuous medium approximation with account for the mutual influence of the electrodynamic, hydrodynamic, and thermodynamic processes typical for the electric discharge, that is, to consider them in the magnetohydrodynamic approximation. A similar approach proved to be efficient when studying the electric discharges in dense gases [6–25]. However, the problem to simulate the electric discharge in a condensed medium in the magnetohydrodynamic approximation is more difficult due to the complicated thermodynamic relations and transport coefficients when the matter's phase state is changed. For example, using such an approach in work [26], a number of adjustable coefficients were introduced into a simplified equation of the water's state, the relations for the specific conductivity, and the plasma's thermal conduction to get reasonable agreement between the estimated values and the experimental results. When simulating the electric discharge at the approximation of the magnetic hydrodynamics, too large a difference between the calculated and the experimental discharge current–time characteristics is recorded in work [27], which shows a considerable energy imbalance within the system.

They managed to solve the problem of such simulation of electric discharges in water using the numerical method of the fully conservative difference schemes [28] providing the maintenance of the energy balance by the types and a wide-range interpolation equation of the water's state [14] in mathematical

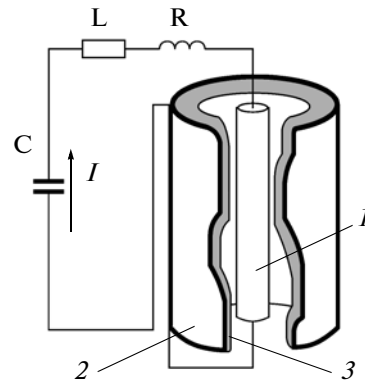


Fig. 1. The equivalent discharge circuit with the capacitive energy storage: C—the bank of capacitors; L, R—the inductance and active resistance of the discharge circuit: (1) the discharge channel; (2) the reverse current lead; (3) the inner wall of the discharge chamber.

model [29] improved in [6, 30]. This work is dedicated to the application of it to analyze the processes in the little volumes of the discharge chambers filled with water.

Thus, the purpose of this work is to analyze the spatiotemporal distributions of the pressure and temperature in a cylindrical discharge chamber considering the interaction between the shock wave excited by the electric discharge in water and repeatedly reflected from the chamber's walls and the plasma channel.

MATHEMATICAL MODEL OF ELECTRICAL DISCHARGE IN WATER

The mathematical model has been published before [6, 30]. Only the main equations that assist in analyzing the processes in a cylindrical discharge chamber filled with water (Fig. 1) are presented in this work. The electrodes connected to the discharge circuit with the capacitive energy storage are arranged along the discharge chamber. The plasma channel is formed between them.

The mathematical model's equations written with the one-dimensional magnetohydrodynamic approximation within the Lagrange coordinate system are as follows:

$$i = \rho \frac{\partial(r^\xi H)}{\partial s}, \quad \mu_0 \frac{\partial}{\partial t} \left(\frac{H}{\rho r^\xi} \right) = \frac{\partial E}{\partial s}, \quad (1)$$

$$i = \sigma E, \quad f = \frac{\mu_0 i H}{\rho}, \quad q = \sigma E^2, \quad (2)$$

$$\frac{\partial}{\partial t} \left(\frac{1}{\rho} \right) = \frac{\partial}{\partial s} (r^\xi v), \quad \frac{\partial v}{\partial t} = -r^\xi \frac{\partial p}{\partial s} + f, \quad v = \frac{\partial r}{\partial t}, \quad (3)$$

“Pop-Out” Effect in ITO/Si and SnO₂/Si Structures

D. Z. Grabko and E. E. Harea

Institute of Applied Physics, Academy of Sciences of Moldova, ul. Akademiei 5, Chisinau, MD-2028 Republic of Moldova
e-mail: evg2000@mail.md

Received July 12, 2012

Abstract—The “pop-out” effect in ITO/Si and SnO₂/Si structures and in silicon used as a substrate is studied. The following pattern is observed for all the materials under study (the ITO/Si and SnO₂/Si structures and the Si substrate): the occurrence of the pop-out effect heavily depends on the maximum applied load (P_{\max}) and less significantly depends on the unloading rate. The internal energy accumulation in the volume beneath the indent should be regarded as a cause of the pop-out effect. In addition, defect structures characteristic of each P_{\max} are formed in the hydrostatic pressure region beneath the indent. These defect structures determine the relaxation pattern during unloading and provide favorable conditions for the occurrence of the pop-out effect. It is shown that there is a certain load range for the Si substrate (40–300 mN) and for the ITO/Si and SnO₂/Si structures (80–400 mN) within which the occurrence of the pop-out effect is most probable.

DOI: 10.3103/S1068375513010043

INTRODUCTION

The pop-out effect in silicon has long been known; it consists in a sudden expulsion of the indenter from the material in a short period of time at the unloading stage. It is evident as a discontinuity in the nanoindentation curve [1–4].

The pop-out effect occurs owing to the phase transformations of the silicon beneath the indenter [5, 6]. The complex mechanism of the deformation of single-crystal silicon results from the formation of a specific defect structure during the indentation, first of all, owing to the phase transformations in the material beneath the indent. At a pressure of 11.3 to 12.5 GPa, the original crystalline silicon (Si-I) undergoes a 22% increase in density and is transformed into Si-II (the β -Sn structure type), which is a metallic phase [6], and it is this that occurs during indentation loading. This phase is unstable; during indentation unloading, it is transformed into the Si-III (the BC8 face-centered structure) and/or Si-XII phases (the R8 rhombohedral structure).

However, along with the above crystalline phases, an amorphous silicon phase (a-Si) is formed in the region beneath the indent. The fraction of the crystalline or amorphous phase formed in the deformation zone beneath the indent largely depends on the maximum applied load [3, 6, 7]. Very low loads (~20 mN) lead to the dominant formation of the amorphous phase, which is shown as an “elbow” effect, i.e., as a curve bend in the form of an “elbow” in the load–displacement curve $P(h)$ during unloading. An increase in the maximum load (~30 mN) results in the formation of a mixed amorphous–nanocrystalline structure. With a further increase in the load, a greater contribu-

tion to the relaxed structure beneath the indent comes from the Si-III and Si-XII crystalline phases. In this case, the pop-out effect is clearly pronounced in the $P(h)$ curve. In the event of the mixed structure, the curves exhibit a combined elbow/pop-out effect.

The final defect structure, as the final phases, depends not only on the applied load but also on the rate of change of the maximum pressure during the unloading. It was found in [4, 6, 7–11] that a slow decrease in the applied load (10–120 mN/min) at the unloading stage stimulates the formation of Si-III and Si-XII structures, and a high rate of decrease in the load (>120 mN/min) contributes to the formation of the amorphous silicon structure (a-Si).

Although the pop-out effect observed in silicon during indentation has been extensively studied, its mechanism is poorly understood and further experiments are required to determine the physical nature of this phenomenon. This problem can be solved using the studies of layer–substrate composite structures in which the substrate is made of silicon.

In accordance with the above, in this study, we analyze the pop-out effect in composite structures in which the substrate is coated with a thin film of either In₂O₃:SnO₂ (ITO) or SnO₂. It is of particular interest to study the phase transformations in ITO/Si and SnO₂/Si structures, because these materials are promising converters of solar energy into electric energy and widely used for the manufacture of solar cells [12–14].

EXPERIMENTAL

The structures were prepared by the spray pyrolysis of an alcoholic solution of indium chloride and tin

chloride (InCl₃ : SnCl₄) in the case of the ITO films and an alcoholic solution of tin chloride (SnCl₄) in the case of the SnO₂ films on a heated silicon substrate [14]. Owing to this, a polycrystalline film of In₂O₃ : SnO₂ (ITO) or SnO₂ with a thickness of 350–400 nm was formed on silicon, which was coated by a ~10-nm-thick SiO₂ oxide layer because of the natural oxidation in the air. The substrates were phosphorus-doped silicon wafers with the (100) crystallographic orientation.

The indentation of the samples of ITO/Si, SnO₂/Si, and single-crystal Si, which was used as a substrate, was carried out using an NHT CSM Instruments SA nanotester. The maximum applied loads (P_{max}) were varied from 5 to 500 mN. Five experiments were carried out for each load. All the measurements on the silicon wafers were conducted in the (100) crystallographic plane. The indentation loading and unloading rate was $2P_{max}/min$. The following mode was used: indentation loading for 30 s, exposure to the load for 20 s, and unloading for 30 s.

To study the effect of the unloading rate on the depth of the occurrence of the pop-out effect, the samples were tested in the same range of maximum loads. The indentation loading rate was $2P_{max}/min$, while the unloading rate remained unchanged for the entire range of the applied loads: it was 80 and 600 mN/min for the low and high unloading rates, respectively.

RESULTS AND DISCUSSION

The pop-out effect in our experiments was observed in the phosphorus-doped silicon wafers (used as a substrate) and during the indentation of the ITO/Si and SnO₂/Si structures. The phenomenon was probabilistic in nature and took place in about 80% of the measurements. The ITO and SnO₂ films had a significant effect on the origin and development of the effect. In this study, the depth of occurrence of the pop-out effect ($h_{pop-out}$) is determined as shown in Fig. 1.

The pop-out effect occurs starting with a maximum applied load of $P_{max} = 40$ mN and above for the ITO/Si structures and starting with $P_{max} = 60$ mN for the SnO₂/Si structures. We believe that this fact is directly related to the presence of Si films on the surface taking into account that, in some cases, the effect occurred on silicon used as substrates at a load of 20 mN. It should be noted that, at $P_{max} < 20$ mN, the pop-out effect was absent in all the experiments either on the ITO/Si or SnO₂/Si structures; instead, an elbow effect took place. The elbow effect occurred in the ITO/Si structures in all the experiments at 20 mN and in two of five cases at 40 mN. In the SnO₂/Si structures, the elbow effect was observed at 20 and 40 mN and even at 60 mN in three of five cases; it gradually gave way to the pop-out effect with increasing loads. The shift of the pop-out effect to higher loads in the ITO/Si and

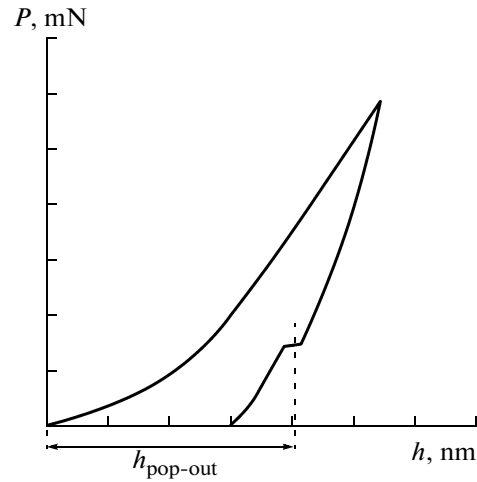


Fig. 1. Graphic representation of the $h_{pop-out}$ value.

SnO₂/Si structures should be apparently attributed to the effect of the ITO and SnO₂ films on the degree of strain of the substrate.

Consider the behavior of a structure composed of a film deposited on a substrate. To deform a silicon substrate to a depth necessary for the occurrence of the pop-out effect, the indenter must overcome the resistance force of the film. During the application of the load to its maximum value, the elastic component of the strain of the films continuously decreases, while the plastic component accordingly increases. This is similar to the fact that, depending on the maximum applied load, the substrate’s structure is subjected to the action of a variable-shape “indenter,” which ultimately affects the maximum penetration depth of the indenter h_m and the distribution of the stress required for a phase transition in the silicon.

Since the hardness of the SnO₂ film is slightly higher than that of the ITO, the occurrence of the pop-out effect on the SnO₂/Si, as stated above, is shifted to higher loads than on ITO/Si.

The results of many studies show that the occurrence of the pop-out effect also depends on the indentation unloading rate [4, 7, 10, 11, 15]. In our experiments, the depth of occurrence of the pop-out was studied for the case in which the time of the loading and unloading remained constant (0.5 min) regardless of the maximum applied load. Thus, the unloading rate was

Table 1. Relationship between the P_{max} value and the indentation unloading rate

P_{max} , mN	20	40	60	80	100	200	300	400	500
v , mN/min	40	80	120	160	200	400	600	800	1000

Derivatographic Studies of a Nanocomposite Based on Polypropylene and D_{K1} Nanogel

M. A. Ramazanov^{a, b}, R. L. Mamedova^b, and A. A. Rasulova^b

^aBaku State University, ul. Khalilova 23, Baku, AZ-1148 Republic of Azerbaijan

^bInstitute of Physics, National Academy of Sciences of Azerbaijan,
pr. Dzhavida 33, Baku, AZ-1143 Republic of Azerbaijan

e-mail: mamed_r50@mail.ru; nanomaterials@bsu.az

Received November 15, 2011; in final form, December 1, 2011

Abstract—Derivatograms of a polypropylene (PP) composite containing 2, 4, and 10 vol % of D_{K1} are represented. Regardless of the crystallization method, all the D_{K1} materials under study undergo a thermal oxidative breakdown at 305–320°C. An increase in the volume content of D_{K1} from 4 to 10% leads to a shift of the depolymerization temperature to higher values, which is most probably attributed to the formation of crosslinked structures in the material. Owing to this, after heating to 500°C, the amount of the solid residue in the PP + 10 vol % D_{K1} material crystallized by rapid cooling achieves 62%.

DOI: 10.3103/S1068375513010110

INTRODUCTION

Derivatographic analysis can be a rapid method of organic synthesis, which gives the possibility to observe the behavior of materials in a wide temperature range using their minimum weighted portions and the possibility to determine the optimum temperature range of the process in the case of intra- or intermolecular interactions in the materials [1]. It is known that the use of different methods of modification of polymer materials leads to a significant expansion of their application range. In addition, a targeted change in the structure and properties of polymers is implemented either during synthesis or through the introduction of fragments of another chemical nature into the macromolecule of the finished product. In designing polymer materials with desired properties, particular attention has been recently given to the modification of their surface, because it is the structure of the surface layer that largely determines their behavior under operation conditions [2–4].

Films of polypropylene (PP) filled with 0.5 and 1 vol % of MnO_2 and subjected to electrothermopolarization were previously studied. Under the action of electrothermopolarization ($E = 7 \times 10^6$ V/m), owing to aging, the crystalline phase of the PP matrix undergoes amorphization resulting in a decrease in the thermal resistance by 40°C compared to the PP samples unexposed to electrothermopolarization. It was found that the electric field effect leads to both the complete amorphization of the PP + 0.5 vol % MnO_2 composite and the complete depolymerization, which is accompanied by the volatilization of 100% of the intermedi-

ates [5]. Based on this, we did not subject the PP + D_{K1} samples to polarization.

EXPERIMENTAL

Powder mixtures of PP and D_{K1} with different ratios of the components were prepared and then subjected to hot pressing (at the melting point of the polymer matrix under a pressure of 15 MPa for 10 min) to produce films of PP + D_{K1} nanocomposites, which were subsequently cooled. The samples were prepared under different temperature–time conditions of crystallization: in a slow cooling mode, in which the samples are cooled to room temperature at a rate of 2°C/min, and in a rapid cooling mode in an ice–water mixture at a rate of 30°C/min. The samples of the films with a D_{K1} filler crystallized under different conditions were examined by derivatography. The derivatograms were recorded using a MOM Q-derivatograph (Hungary) with the following channel sensitivity: DTA, 1/5; DTG, 1/15; TG, 20 mg; a weighted portion of 150 mg. The samples were heated in the temperature range of 20–500°C at a heating rate of 20°C/min [6].

RESULTS AND DISCUSSION

Figure 1 depicts derivatograms of PP composites containing 2 and 4 vol % of D_{K1} , which were crystallized by rapid cooling. The parameters of the changes in the thermal characteristics of the PP after filling with 2, 4, and 10 vol % of D_{K1} are listed in the table. According to these data, after crystallization by rapid cooling under different conditions, the samples were

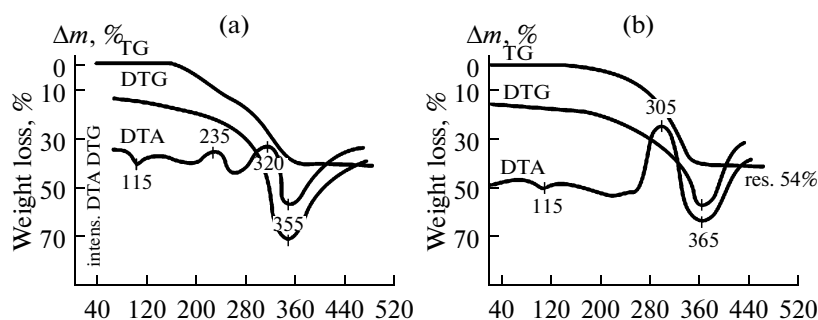


Fig. 1. Derivatograms of (a) the PP + 2 vol % D_{K1} and PP + 4 vol % D_{K1} nanocomposites prepared by rapid cooling.

prepared through the introduction of up to 10 vol % of D_{K1} into the PP. For the DTA curves (Figs. 1, 2), it is found that the introduction of up to 2 vol % of D_{K1} into the PP in the rapid cooling mode leads to a decrease in the crystalline phase of the matrix with $T_{melt} = 115^{\circ}\text{C}$, as evidenced by the low-intensity endothermic effect in the DTA curve (Fig. 1a); as the concentration of D_{K1} increases to 4 vol %, the intensity of the endothermic effect in the DTA curve further decreases (Fig. 1b). These curves (Figs. 1, 2) suggest that the crystalline phase of the matrix undergoes amorphization, which results in a decrease in its amount.

It is also evident from the figures that, with a further increase in the filler concentration to 10 vol % (Fig. 2b), the intensity of the melting point of the crystalline phase of the matrix slightly increases, although the melting temperature decreases to 107°C compared to that of the PP samples containing 2 and 4 vol % of D_{K1} . An analysis of the composites crystallized by rapid cooling, which contain 2, 4, and 10 vol % of the D_{K1} filler, suggests that the decrease in the amount of the

crystalline phase of the matrix results from the structural changes in the polymer at the molecular and supramolecular levels induced by the effect of the D_{K1} additive particles. In the case of crystallization of PP + 10 vol % D_{K1} in nitrogen and by slow cooling (Figs. 2a, 2c), the composite undergoes amorphization, as evidenced by the absence of endothermic effects corresponding to the melting of the crystalline phase of the matrix in the DTA curves (Figs. 2a, 2c).

The table shows that, in the case of crystallization by rapid cooling, the temperature of the thermal oxidative breakdown in the PP + 10 vol % D_{K1} material has increased by 20°C compared to the PP + 2 vol % D_{K1} composite; this can be attributed to the formation of electrically nonequilibrium fragments, which are the active sites at which the thermal oxidative breakdown reactions of macromolecules are localized. Regardless of the crystallization method, thermal oxidative breakdown occurs at $305\text{--}320^{\circ}\text{C}$ in all the materials under study. An increase in the D_{K1} content from 4 to 10 vol % leads to a shift of the depolymeriza-

Thermal parameters of the PP composites with a D_{K1} nanogel filler under different crystallization conditions

Content of filler in the PP + D_{K1} materials, vol %	Crystallization mode	Differential thermal analysis DTA			Differential thermogravimetric analysis DTG, TG			
		Endothermic effect	Exothermic effect, $T^{\circ}\text{C}$	Endothermic effect $T^{\circ}\text{C}$, DTG	Gas volatilization temperature range according to the TG, $T^{\circ}\text{C}/\%$			Residue, %
2	Rapid cooling	$T_{melt} = 115$, $T_{depol} = 355$	235; 320-thermal oxidation	355	170–235/7.2	235–262/7.2	262–355/26.0	59.6
4	Rapid cooling	$T_{melt} = 115$, $T_{depol} = 365$	305-thermal oxidation	365	175–260/6.0	260–305/5.0	305–365/35.0	54.0
10	Rapid cooling	$T_{depol} = 390$	310-thermal oxidation	390	170–290/7.7	290–310/4.4	310–390/33.0	55.0
10	In nitrogen	$T_{melt} = 107$, $T_{depol} = 375$	255; 315-thermal oxidation	265; 370	165–265/8.0	265–335/7.0	335–375/23.0	62.0
10	Slow cooling	$T_{depol} = 370$	315-thermal oxidation	370	195–255/5.0	255–315/9.0	315–370/27.0	59.0

A Microscopic Study of the Effect of γ -Radiation on $\text{Pb}_{1-x}\text{Mn}_x\text{Se}$ Epitaxial Films

I. R. Nuriev^a, R. M. Mamishova^b, N. N. Gadzhieva^b, M. A. Ramazanov^c, and R. M. Sadygov^a

^a*Institute of Physics, National Academy of Sciences of Azerbaijan, pr. Dzhavida 33, Baku, AZ-1143 Republic of Azerbaijan*

^b*Institute of Radiation Problems, National Academy of Sciences of Azerbaijan, ul. Vagabzade 9, Baku, AZ-1143 Republic of Azerbaijan*

^c*Baku State University, pr. Dzhavida 23, Baku, AZ-1148 Republic of Azerbaijan*

e-mail: asi_mr@mail.ru; rexsane@yandex.ru

Received December 1, 2011; in final form, April 6, 2012

Abstract—The surface morphology of *n*- and *p*-type epitaxial films of lead manganese selenide ($\text{Pb}_{1-x}\text{Mn}_x\text{Se}$ ($x = 0.01$)) on barium fluoride substrates of the (111) orientation in the initial state and after exposure to gamma-radiation is studied by atomic force microscopy. It is shown that the surface relief undergoes modification in the absorbed dose region of $5 \leq D_\gamma \leq 35$ kGy. The $p \leftrightarrow n$ conductivity inversion at $10 \leq D_\gamma \leq 25$ kGy is found from the characteristics of the surface structures and confirmed by the electrophysical measurements. It is revealed that the radiation resistance of these films is violated at a dose above 35 kGy.

DOI: 10.3103/S1068375513010092

INTRODUCTION

The search for radiation-resistant materials of various types and the development of new optoelectronic devices operating in the infrared spectrum based on these materials are important challenges facing modern science and technology. Among these materials, $\text{A}^{\text{IV}}\text{B}^{\text{VI}}$ compounds and their solid solutions are of particular interest. The presence of ions of heavy metal elements (lead, tin) in the crystal lattice of semiconductors of this type provides the high radiation and thermal stability of the devices prepared on their basis. For a long time, the above semiconductor compounds and their solid solutions have been extensively used in devices of infrared technology operating in the wavelength range of 3–5 and 8–14 μm [1]. Thus, a technique for the preparation of epitaxial films of these materials with a high degree of crystalline perfection on various substrates has been developed in recent years [2–9]. In particular, they include epitaxial films of $\text{Pb}_{1-x}\text{Mn}_x\text{Se}$ solid solutions. The manganese ions in the composition of these solid solutions impart new properties that are characteristic of semimagnetic semiconductors and offer many possibilities for designing magnetic diodes on their basis that operate in the IR wavelength range of 3–5 μm [10–11]. Since modern optoelectronic devices are mostly prepared on the surface of crystals, the surface diagnostics assume great importance [12]. The monitoring of gamma-radiation induced changes in the surface and the choice of the performance characteristic of diodes based on these solid solutions taking into account the effect of the observed changes on their physical properties make it possible to predict the operating modes

of the diodes. In this respect, it is of particular interest to study the changes in the surfaces of $\text{Pb}_{1-x}\text{Mn}_x\text{Se}$ ($x = 0.01$) epitaxial films exposed to gamma-radiation in comparison with the original samples. In this study, we derived three-dimensional (3D) images of the surface and size distribution curves of the surface image elements, i.e., histograms for the original $\text{Pb}_{1-x}\text{Mn}_x\text{Se}$ ($x = 0.01$) epitaxial films and the ones exposed to gamma-radiation ($D_\gamma = 5\text{--}35$ kGy).

EXPERIMENTAL

$\text{Pb}_{1-x}\text{Mn}_x\text{Se}$ ($x = 0.01$) epitaxial films were prepared on (111) BaF_2 substrates by molecular beam condensation at a pressure of 10^{-4} Pa using a UVN71-R3 standard vacuum system. Synthesized $\text{Pb}_{1-x}\text{Mn}_x\text{Se}$ ($x = 0.01$) solid solutions were used as the source. The perfection of these films was studied by electron diffraction, electron microscopy, and X-ray diffraction. The degree of the crystalline perfection, i.e., the full width at the half maximum of the X-ray rocking curves expressed in arc seconds, was determined using a TRS triple-crystal X-ray spectrometer and a DRON-3 instrument. The electron diffraction pattern of the reflections from the $\text{Pb}_{1-x}\text{Mn}_x\text{Se}$ films was derived using an EMR-100 electron diffractograph (Fig. 1a) and interpreted to determine the cell parameter ($a = 6.11$ Å). According to the developed technique using an additional source of Se, *n*- and *p*-type epitaxial films with a cubic structure ($a = 6.11$ Å), a thickness of 0.5–1 μm , a high degree of crystalline perfection ($W_{1/2} = 90\text{--}100''$), and high electrophysical parameters ($\mu_{n,p}(77\text{ K}) = (2.5\text{--}3) \times 10^4 \text{ cm}^2/(\text{V s})$) were grown

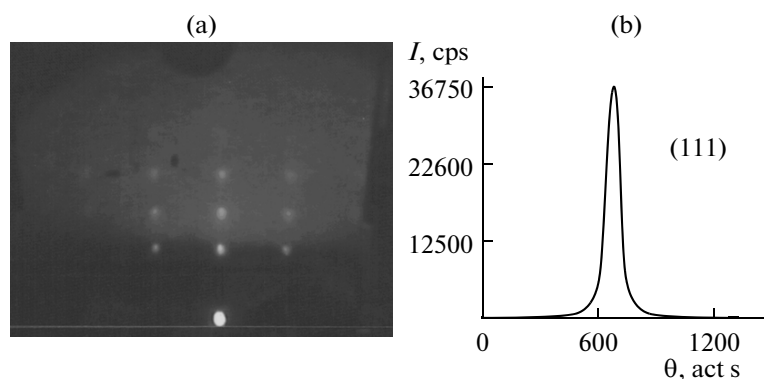


Fig. 1. (a) Electron diffraction pattern and (b) X-ray diffraction curve of the $\text{Pb}_{1-x}\text{Mn}_x\text{Se}$ ($x = 0.01$) epitaxial films.

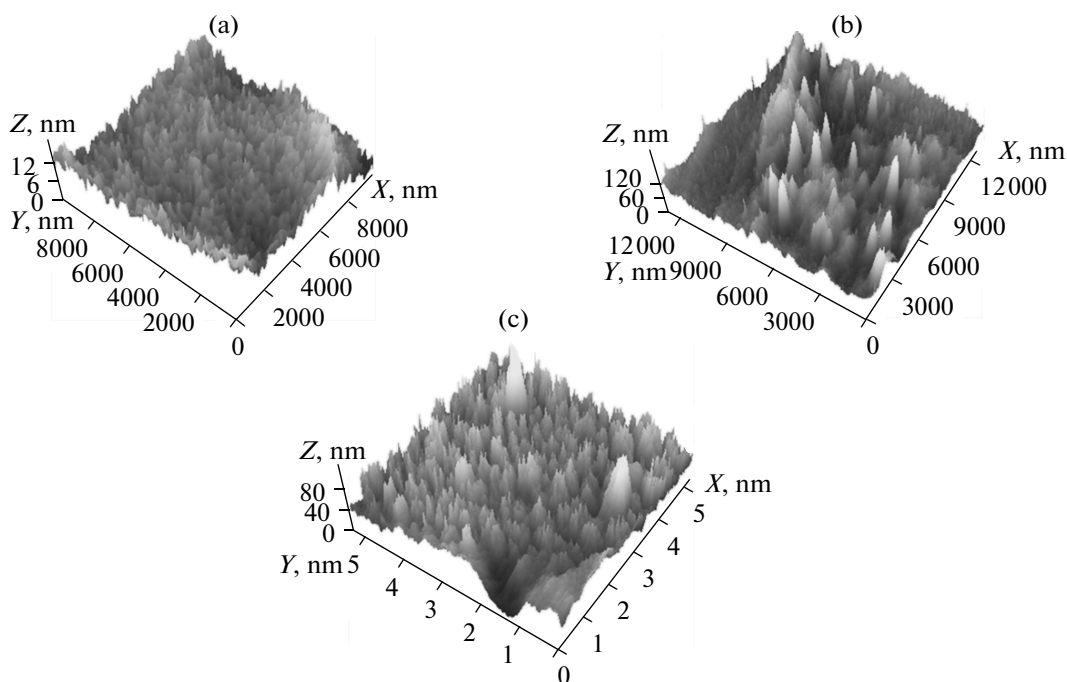


Fig. 2. 3D AFM images of the surface of the n -type $\text{Pb}_{1-x}\text{Mn}_x\text{Se}$ ($x = 0.01$) epitaxial films (a) before and after exposure to gamma radiation at $D_\gamma =$ (b) 10 and (c) 25 kGy.

(Fig. 1). The electrophysical parameters (conductivity, Hall voltage) of the films prepared on dielectric substrates were measured by the potentiometric method in a constant magnetic field of 2500 Oe in a cryostat evacuated to 2×10^{-4} mmHg at the boiling point of liquid nitrogen (77 K).

The resulting samples were exposed to a dose of $D_\gamma = 5\text{--}35$ kGy using an MRX γ -25 setup with a Co^{60} isotope source ($E = 1.25$ MeV). The absorbed dose rate of the source was $dD_\gamma/dt = 0.40$ Gy/s. The surfaces of the epitaxial films before and after their exposure to the gamma radiation were studied using an SZMU-L5 atomic force microscope (AFM). 3D images of the surfaces of the films, their histograms, and their Fourier spectra were obtained. The conductivity inversion

in the irradiated samples was monitored by microscopic and electrophysical methods.

RESULTS AND DISCUSSION

The original surfaces of the lead manganese selenide epitaxial films and the changes occurring on the surfaces of these samples after their exposure to gamma radiation were examined using an AFM. To determine the dynamics of the morphological changes in the surfaces and study the postirradiation effects, i.e., the effects observed after the cessation of the exposure of the samples to γ -rays, we derived 3D surface images and their histograms (size distribution curves of the surface image elements) of the n - and p -type epitaxial films, which are shown in Figs. 2–5.

Experiments on the Advantages and Limits of Using Conventional Friction Welding for Joining Dissimilar and Graded Materials¹

I. Mitelea, V. Budău, C. Dorohoi, and C. M. Crăciunescu

“Politehnica” University of Timisoara, P-ta Victoriei nr. 2, Timisoara, 300006, Romania

e-mail: ion.mitelea@mec.upt.ro

Received February 14, 2012

Abstract—Investigations concerning opportunities to apply the friction welding technique for joining dissimilar and graded materials are considered, starting from the advantages offered by this process in assembling parts for manufacturing equipments parts and automotive industry components. Experiments have been carried out on friction welding of heat treated 42CrMo4 with C45 steel and with the solution treated X6CrNiTi18–10 steel, as well as on joining copper with Al alloys. Metallographic observations and hardness measurements are performed in order to detail the peculiarities of the process of making joints that are difficult to obtain by conventional electric arc welding.

DOI: 10.3103/S1068375513010080

INTRODUCTION

Friction welding is a technique that relies on thermomechanical processes, known to lead to significant structural changes in steels and other metallic materials [1], located at the interface of the joint. Several currently used types of friction welding are: stir, rotational, linear, and orbital welding. Nowadays friction stir welding (FSW) attracts most attention in the scientific world [2], with its significant opportunities for practical applications extended to a variety of materials, even steels [3]. FSW is a process that can be used to repair surface and near surface defects, and increase material strength. It is based on heating by friction and the subsequent plastic deformation of a workpiece placed between a rotating tool and the mating surfaces of the welded parts. The rotating tool is plunged in the material and then shifts along the joining line with a linear speed. The plasticized material is transferred beyond the tool, thus leading to the welded joint. FSW is a complex process, still under development for joining similar materials, and its complexity is reflected by thermomechanical modeling of phenomena. The following are the most relevant advantages of FSW [4]:

- subsequent machining is not necessary;
- lower energy requirement;
- welds of materials with different geometries can be made;
- long welding seams are possible.

However, the FSW process has also some limitations in contrast to conventional friction welding. They are:

- reduced number—so far—of the couples of materials that can be joined;
- specific requirements for clamping of workpieces;
- significant wear and cost of the rotational tool;
- difficulties in processing of the coated material;
- lower productivity for joints made in a single step.

Thus, rotational friction welding, also known as conventional friction welding, still keeps a significant segment among currently used techniques, while continuously expanding to include both similar and dissimilar materials [5, 6], thus offering substantial advantages compared to resistance and arc-welding techniques. The main characteristics of the joint, from the point of view of its constructive design, are related to the geometry of the weld. Dimensional coaxial or along the length misfits are significantly less than 0.5 mm, depending on the performances of the welding equipment.

Among the main aspects, concerning the friction-welded joints, are [7–9]:

- the expungement of the material initially in contact does not require pre-cleaning of the surfaces to be welded;
- the resulting mechanical strength is equal or higher than the one of the base material;
- the heated and mechanically affected zones are less extended and their mechanical characteristics less degraded;
- the microstructure of the joint plane shows a finer structure than the one of the base materials;

¹ The article is published in the original.

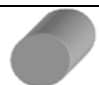











Shapes	Examples			
Typical				
Hollow				
Less common				

Fig. 1. Cross-section of weldable geometries.

—an adequate forging expunges the overheated austenitic grains in the outer area and generates a grain refinement in the welded joint;

—the strength of the joint for dissimilar materials is at least equal to the lesser strength of the welded materials;

—there is no risk for decarburation of the steel parts to be welded.

The mechanical characteristics of the friction-welded joints are superior to the ones of the base materials, due to the favorable effects of the thermo-mechanical treatments during the process. In addition, the heat affected zone (HAZ) is less extended compared to that in other welding techniques, and the presence of segregations and porosities can be avoided in the joining plane.

The present work specifies the opportunities of application of the conventional friction welding process for joining similar, and especially, dissimilar materials. It also is an investigation on the welding behavior of nonferrous metals and alloys, which causes difficulties in making joints using the arc melting process.

A FRICTION WELDING APPROACH FOR INDUSTRIAL PROCESSES

According to the conventional friction welding process requiring rotation of the parts, the geometry of the components should show at least a contact surface with rotational symmetry. In principal, parts with solid and hollow sections can be welded, and depending on the rigidity of the walls, they can also be welded to flat surfaces. Figure 1 presents some of the geometries of the cross-section of the components that can be welded.

The implementation of friction welding technology usually arises from a metallurgical need or has an economical justification, allowing the optimization of the technological process and the reduction of cost. Several applications of the conventional friction welding process are highlighted in table.

On the other hand, the friction welding process is sometimes limited or more difficult to implement for

materials that show inhomogeneities and compositional gradients, especially in the joining plane [8–11]. Sometimes, depending on the couple of materials to be joined, post-welding treatments may be required. For joining dissimilar materials that are metallurgically incompatible, the formation of intermetallic compounds in the seam can be avoided by using intermediate layers.

The conventional friction welding process parameters (axial pressure, rotational speed, processing time) can be easily adjusted. They determine the initiation and the ending of the welding process, leading to high quality joints with reproducible properties. Beside those parameters, and in order to avoid cracking and fractures, supplementary precautions can be prescribed, related to preheating, cooling rates and subsequent heat treatments for tempering and stress relief. Compared to other welding techniques, friction welding is a solid-state process that does not require melting and offers relevant advantages related to the quality of the joint, the lack of additional materials, fluxes and protection gases. It is also economical, with such benefits as: lower energy consumption, reduced costs for surface preparation and subsequent machining, short welding times and high productivity, fewer human errors and no ecological risks.

EXPERIMENTAL DETAILS AND RESULTS

The friction welding experiments were performed using the equipment with the schematic principle and the practical solution depicted in Fig. 2. Structural observations of a dissimilar weld between heat treated 42CrMo4 low-alloyed steel and a C45 carbon steel are shown in Fig. 3.

The interface is an un-deformed plane—suggesting limited thermo-mechanical differences between the steels—that reveals the HAZ in each steel (Fig. 3a).

Experiments performed on joining stainless to mild alloyed or unalloyed steels are especially important for recipients operating under pressure. Mild alloys have a ferritic structure, while the Cr–Ni or Cr–Ni–Mo show an austenitic structure. Such joints are named “black-and-white” joints. A joint made out of the quenched-tempered 42CrMo4 and solution treated X6CrNiTi18–10 steels by friction welding was also subject to experiments. The main friction welding parameters for the “black-and-white” joint are: $n = 2900$ turns/min.; friction pressure 40 N/mm^2 ; upsetting pressure 45 N/mm^2 ; friction time 3.5 s ; deceleration time 0.09 s ; upsetting time 3.2 s .

The results of the friction welding process are shown in Fig. 4. The hardness gradient across the joining plane is detailed in Fig. 5.

The difficulties arising in welding processes requiring melting are related to the significant micro-structural differences. Thus, mild steels require preheating and cooling with a relatively low cooling rate of the

Evolution of a Thermal Field in a Homogeneous Conductor when Non-Stationary Heated by a Flowing Current

A. G. Merkushev and M. A. Pavleyno

Electrophysics Research and Education Center of the Physics Department, Saint Petersburg State University,
ul. Ul'yanovskaya 3, Petrodvorets, Saint Petersburg, 198504 Russia

e-mail: alexey.merkushev@gmail.com, pmf@nm.ru

Received February 28, 2012

Abstract—This paper offers an analytical solution to the temperature distribution problem in a one-dimensional current-carrying conductor. The proposed solution is compared to the numerical solution obtained with the finite-element method. When considering the temperature distribution evolution problem in current-carrying systems, a real system has been replaced with a system of one-dimensional current-carrying conductors and concentrated contact resistances.

DOI: 10.3103/S1068375513010079

INTRODUCTION

Elements of current-carrying systems incorporated in electrical installations are sometimes exposed to impulses of current exceeding the nominal value. Such situations take place, for example, when starting an electric engine, if a short-circuit occurs, and in some other cases. This leads to additional heating of the conductors. The maximum permissible levels of heating are established by the corresponding design rules [2]. It is important to be able to make the necessary calculations of the temperature regimes of a current-carrying system when it is subjected to nonstationary heating. In general, this problem requires a great amount of numerical calculations in a three-dimensional state space, which can be performed in modern CAD/CAE systems, for example, Comsol, ANSYS, etc. Examples of these calculations can be found in [3–4]. However, we notice such techniques are rather difficult and computationally expensive.

In some cases, a simplified approach is efficient, which is based on assuming the original system to be a one-dimensional model representing one-dimensional conductors connected to each other by contact resistances. This technique was used in [1] for the case of heating by a rated current. In the present paper, a generalization of the mentioned approach to the nonstationary heating case is presented. An analytical solution describing a thermal field's evolution in a one-dimensional conductor was obtained and validated through the comparison of the obtained solution to the results of numerical simulations.

We shall give a mathematical formulation of a temperature distribution problem in a one-dimensional current-carrying conductor:

$$\rho C \frac{\partial}{\partial t} T = \frac{\partial}{\partial x} K \frac{\partial}{\partial x} T \quad (1)$$

$$+ \rho_{e0} (1 + \alpha(T - T_{pe0})) j^2 - \sigma(T - T_{ref}),$$

$$\left(-K \frac{\partial T}{\partial x} S \right)_{x=0} = H_l(t), \quad (2)$$

$$\left(K \frac{\partial T}{\partial x} S \right)_{x=L} = H_r(t), \quad (3)$$

$$T_{t=0} = T_{init}. \quad (4)$$

Equation (1) is a one-dimensional heat equation taking into account the Joulean heat generation and the linearized losses through the lateral surface. Boundary conditions (2) and (3) determine the heat flows at both ends of the conductor. The initial condition (4) suggests that the conductor was heated uniformly to a certain temperature T_{init} before the current was switched on.

Here, T is the temperature (the function sought for), t is the time, x is the coordinate along the one-dimensional coordinate system, ρ is the density, C is the specific heat capacity, K is the thermal conductivity, ρ_{e0} is the specific electric resistance at the temperature of T_{pe0} , α is the temperature resistance coefficient, j is the current density, σ is the coefficient characterizing the heat exchange between the conductor and the environment through the lateral surface, T_{ref} is the ambient temperature, L is the length of the con-

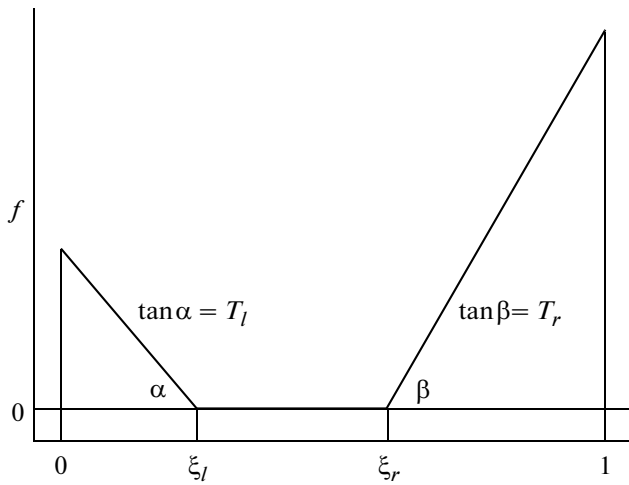


Fig. 1. Outlined graph of the function f .

ductor, S is the cross sectional area, $H_l(t)$ is the input heat flow at the left end of the system, and $H_r(t)$ is the input heat flow at the right end of the system.

CONSTRUCTING THE ANALYTICAL SOLUTION

We suggest that the heating temperature does not exceed the temperature of the softening of the material, and such physical parameters as the density, heat capacity, and thermal conductivity are constant. At the same time, the specific electric resistance's dependence on the temperature cannot be neglected since its value varies substantially under the given heating. In total, assuming that the heat losses through the lateral surface of the conductor are linear, Eq. (1) can be written as

$$\frac{\partial T}{\partial t} = \chi \frac{\partial^2 T}{\partial x^2} + w_1 T + w_0. \quad (5)$$

In Eq. (5), $\chi = K/(\rho C)$ is the thermal conductivity and

$$w_0 = (\rho_{e0}(1 - \alpha T_{\rho_{e0}})j^2 + \sigma T_{\text{ref}})/(\rho C),$$

$$w_1 = (\rho_{e0}j^2 \alpha - \sigma)/(\rho C).$$

To obtain Eq. (5) in dimensionless variables, we introduce the dimensionless coordinate $\xi = x/L$ and the dimensionless time $\tau = t/t_{\text{max}}$, where t_{max} is the upper limit of the finite time interval of the considered process. Moreover, the sought function may be conveniently changed to $T = \hat{T} - w_0/w_1$, which leads to a homogeneous equation. Finally,

$$\frac{\partial \hat{T}}{\partial \tau} = \theta_1 \frac{\partial^2 \hat{T}}{\partial \xi^2} + \theta_2 \hat{T}. \quad (6)$$

In Eq. (6), the notations $\theta_1 = \chi t_{\text{max}}/L^2$ and $\theta_2 = t_{\text{max}}w_1$ are used. The mentioned parameters carry information about the system's properties.

Using dimensionless coordinates for boundary conditions (2) and (3), we obtain

$$-\left(\frac{\partial \hat{T}}{\partial \xi}\right)_{\xi=0} = R_l H_l(t), \quad (7)$$

$$\left(\frac{\partial \hat{T}}{\partial \xi}\right)_{\xi=1} = R_r H_r(t). \quad (8)$$

In Eqs. (7) and (8), the notation $R_l = L/(KS)$ is used to introduce the thermal resistance according to its dimension. Assuming $T_l(t) = R_l H_l(t)$ and $T_r(t) = R_r H_r(t)$, we simplify Eqs. (7) and (8).

Taking into account that the sought function was changed, initial condition (4) is given by the equation

$$\hat{T}_{\tau=0} = T_{\text{init}} + w_0/w_1. \quad (9)$$

Thus, we have problem (6)–(9) stated with dimensionless variables. To solve the initial boundary value problem with inhomogeneous boundary conditions, we use the reduction of the boundary conditions. Make another one a modification of the sought function:

$$\hat{T} = \tilde{T} + f(\xi),$$

$$f(\xi) = \theta(\xi_l - \xi)(\xi_l - \xi)T_l + \theta(\xi - \xi_r)(\xi - \xi_r)T_r, \quad (10)$$

where $f(\xi)$ should be deliberately chosen so that \tilde{T} can satisfy the homogeneous boundary conditions. In Eq. (10), $\theta(\xi)$ is the Heaviside function, and the points ξ_l and ξ_r belong to the interval $(0; 1)$ and satisfy the inequality $\xi_l \leq \xi_r$. The graph of $f(\xi)$ is shown in Fig. 1 to grasp a better idea of the function.

After the function was modified, Eq. (6) is written as

$$\frac{\partial \tilde{T}}{\partial \tau} = \theta_1 \frac{\partial^2 \tilde{T}}{\partial \xi^2} + \theta_2 \tilde{T} + g(\xi) + h(\xi). \quad (11)$$

In Eq. (11), the following notations are used:

$$g(\xi) = \theta(\xi_l - \xi)(\xi_l - \xi)\left(\theta_2 T_l - \frac{dT_l}{d\tau}\right) + \theta(\xi - \xi_r)(\xi - \xi_r)\left(\theta_2 T_r - \frac{dT_r}{d\tau}\right), \quad (12)$$

$$h(\xi) = \theta_1 (\delta(\xi_l - \xi)T_l + \delta(\xi - \xi_r)T_r). \quad (13)$$

In Eq. (13), $\delta(\xi)$ is the Dirac delta function.

The Possibility of the Application of Amorphous Micro- and Nanowires with the Barkhausen Effect

S. A. Baranov^{a, b, c}

^a*Institute of Applied Physics, Academy of Sciences of Moldova, ul Akademiei 5, Kishinev, MD-2028 Republic of Moldova*

^b*Shevchenko Pridnestrovskii State University, ul. 25 Oktyabrya 128, Tiraspol', Republic of Moldova*

^c*Department de Genie Physique, Ecole Polytechnique de Montreal, C.P. 6079, succ. Centre-ville, Montreal H3C 3A7, (Quebec) Canada*

e-mail: baranov@phys.asm.md

Received February 28, 2012

Abstract—The possibility of the application of the Barkhausen effect arising with the use of magnetic micro- and nanowires is studied. These wires are characterized by a rectangular hysteresis loop and can be used in measuring and identification equipment and in medicine.

DOI: 10.3103/S106837551301002X

INTRODUCTION

It is known that a cast amorphous microwire in glass encapsulation (CAMGE) with positive magnetostriction possesses a rectangular hysteresis loop and its magnetization is reversed by a large Barkhausen jump (LBJ), the coercive force of which can be regulated by both the residual and external mechanical stresses (see, e.g., [1–3]). The increase in the residual or externally applied longitudinal stresses leads to an increase in the coercive force. In our opinion, this acts as one more proof of the longitudinal magnetic structure in the CAMGE with positive magnetostriction proposed in [3]. Although this is experimentally and theoretically proved in [4–10], up to now a number of the aspects discussed are questionable (see, e.g., [1, 2]). In this work, we will continue the discussion started in [3] about the possible magnetic structures in amorphous micro- and nanowires and their influence on the magnetic characteristics.

Various wires (including micro- and nanowires) feature properties of magnetization reversal with the use of LBJ, and their magnetic structure can differ from the magnetic structure of the CAMGE. In this case, the possibility of their long-term existence in certain (one of two) magnetized states and the step-wise transition from one magnetized state to another is called the magnetic bistability effect (by analogy with similar effects in other sections of physics). However, as was already noted in [3], the particular domain structure of these micro- and nanowires can differ from one another. Therefore, a wider theoretical study of the bistability phenomenon in magnetic materials that will not depend on the particular magnetic structure makes some sense.

Bistable ferromagnet (BF) technology is usually reduced to its formation in material with a strongly pronounced gradient of the magnetic potential profile, which is possible, e.g., in CAMGE, in the presence of quasi-mono-axial magnetic anisotropy. Then, both bistable states can be abstractedly represented as energy levels of the system spaced by the energy barrier. BFs were earlier obtained by thermal and mechanical treatment. Thus, in particular, the well-known Wiegand vicalloy wire was obtained [11–15]. In contrast to the Wiegand wire, since the production moment, the CAMGE with a positive magnetostriction is a BF.

In addition to the CAMGE manufacturing technology, there is the Unitika technology (Unitika Ltd.). The wires manufactured by the Unitika technology (this technology is also called in rotating water quenching) possess another magnetic structure [3] and different (from CAMGE) magnetic characteristics, although they are also referred to BF. Moreover, there are chemical and electrochemical methods of depositing nanowires and obtaining nanoparticles by the spark method [16, 17]. A number of materials obtained by these technologies can also be BFs.

The properties of CAMGE are basically discussed in this work, but our many results can be referred to any BF. We will start to discuss the magnetization reversal mechanisms, which were opened, in particular, in studies of the magnetization reversal of materials out of the Wiegand vicalloy wire [12–15] and earlier in studies of multiple-jump materials [18] and theoretically studied in detail in [19]. In our opinion, it is necessary to theoretically analyze the experimental results obtained in [1, 20] from this position.

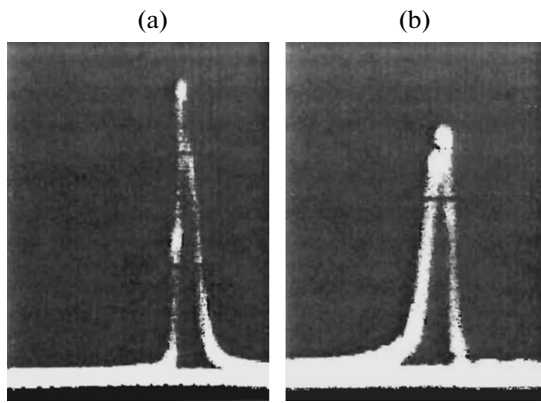


Fig. 1. (a) Relaxational and (b) accelerative pulse forms [3, 4]. They are plotted along the axes (in arbitrary units): X is the time at the Barkhausen jump moment (when the external field's intensity slowly increases with time according to the linear law and reaches the starting field), and Y is the response of the magnetic induction arising at the BF magnetization reversal.

TWO MAGNETIZATION REVERSAL PULSE FORMS

The study of two Barkhausen jump forms as two independent magnetization reversal mechanisms was started, as we know, in work [18], where, in particular, the single pulse structure in multiple-jump magnets was studied. When multiple-jump magnetization reversal forms of the magnets are studied, it is very difficult to analyze single jumps (the experimental problems are discussed in [18]). It followed from the results of [18] that, along with the simple 180° and 90° movement of the domain boundaries, which are retarded by defects, there are the magnetization reversal forms due to the interaction of these boundaries leading to an abnormal magnetization jump but physically to the stepwise domain reorganization. Just this magnetization reversal was later called relaxational (the term is related to the fact that the possibility of a similar relaxation to a more stable domain structure was discussed in [18]).

If the structure of single pulses in the BF, as the CAMGE, is studied, one can find out [3, 4] that the BF magnetization reversal is also carried out by two mechanisms, which, by analogy with [18] (and [13–15]), were called relaxational and accelerative. The relaxational mechanism is characterized by a pulse with a steep leading edge and a gentle falling edge, and the accelerative mechanism is characterized by a smooth increase and a sharp fall of the second leading edge of the pulse (see Fig. 1).

The analysis of the studies shows that the operating characteristics of the BF in which these mechanisms show themselves are ambiguous. Therefore, it is necessary to study in detail the usefulness of the first or second type of pulses (or even their combinations). Work [13] was one of the first studies in which attention was paid to the need for the similar analysis of two

Barkhausen jump (BJ) forms. In addition, it was noted that, in a deformed Wiegand wire (namely, it was studied in [13]), the second form of the magnetization reversal pulse was more stable (according to [13], the fluctuation of the parameters did not exceed 4%). Moreover, the accelerative movement form was also characterized by a sufficiently high pulse duration ($\sim 50 \mu\text{s}$) and a relatively small starting field (as compared with the relaxation movement's form).

It was established in the CAMGE [3, 4] that a more stable magnetization reversal form is related exactly to the relaxational form (in contrast to a Wiegand wire). At the same time, the magnetization reversal mechanism (according to [3]) was carried out in a certain sequence. The magnetization reversal started inside the microwire, where the magnetic anisotropy is lower, and the domain wall formed there probably propagated in an accelerative way. This process corresponded to the nucleation of the magnetization reversal, and, in certain magnetization reversal conditions, it could fail to show itself (e.g., due to a small starting field and a small relative volume of the switched material). Then, the relaxation jump of the magnetization reversal pulse occurs through the potential barrier, which also ends with the possible accelerative movement of the domain wall. If closure domains are created at the ends of the studied CAMGE section [3, 4], with their specified sizes, the accelerative movement form of the domain wall was suppressed. Then, the relaxation movement form played the main part in the magnetization reversal process, which is more stable in the CAMGE case. One can make a competent assumption that the relaxation magnetization reversal form will play an even more important part when the sizes of the microwire's diameter are decreased (in its moving to a nanowire).

Since we assume that the relaxation magnetization reversal movement's form can be actually independent of the movement of the domain wall, which is always accompanied by the presence of eddy currents, it is possible to more simply describe the magnetization reversal process of the dipole of the micro- and nanowires, which will be further considered.

THE FIELD OF THE MAGNETIC DIPOLE SWITCHED BY THE RELAXATIONAL METHOD

Regardless of the magnetization reversal mechanisms considered the above, an important problem is to increase the operation distance, i.e., the distance from the BF magnetic dipole radiating the signal to the transducer reading the signal, which arises due to the BF magnetization reversal using the LBJ. The magnetic quantity devices possess a sufficiently high sensitivity to fixed and alternating magnetic fields. Induction coils are the most simple and sensitive to the alternating fields, and, for efficiency, they can be equipped with ferrite rods (a similar unit is often called a *magnetic antenna*), but the magnetomodulation transduc-

Electrode Material for Supercapacitors Based on Nanostructured Carbon

S. L. Revo^a, I. M. Budzulyak^b, B. I. Rachiy^b, and M. M. Kuzishin^b

^a*T. Shevchenko Kiev National University, ul. Vladimirskaya 64, Kiev, 01601 Ukraine*

^b*V. Stefanyk Ciscarpathian National University, ul. Shevchenko 57, 76025 Ivano-Frankovsk, Ukraine*

e-mail: revo@univ.kiev.ua

Received March 6, 2012; in final form, March 22, 2012

Abstract—Results are presented of studies of composite materials based on nanoporous carbon for application as an electrode material for supercapacitors with an aqueous KOH electrolyte solution. The optimum concentration ratio of the formula components for the electrode material is found on the basis of the studies of the power–capacitance characteristics of the studied samples of such capacitors.

DOI: 10.3103/S1068375513010122

INTRODUCTION

The rampant development of portable electronic devices, hybrid transport vehicles, and backup power supply units requiring new power sources with improved specific characteristics, larger operating times, and enhanced reliability has been observed recently. Such power sources must be cheap, lightweight, and readily accessible. The most promising power sources as regards the service life, the amount of charging–discharge operating cycles, and also the maximum power density are electrochemical capacitors.

According to Conway [1], electrochemical capacitors or supercapacitors (SCs) are electrochemical devices in which quasi-reversible electrochemical charge–discharge processes occur. The shape of the galvanostatic charge and discharge curves of these processes is close to linear, i.e., close to the shape of the corresponding dependences for usual electrostatic capacitors. SCs consist of electrodes based on materials with a developed inner surface separated by a separator and placed into a sealed case. The internal medium of SCs is filled with an electrolyte. Thus, a supercapacitor consists of two capacitor electrodes serially connected through a resistance. The main factors affecting the SC parameters are as follows: firstly, the physicochemical properties of the active electrode material and, secondly, the composition of the electrolyte, separator, and the current collector. In addition, an important role is played by the structural elements of the electrodes, the case, the methods of sealing, etc.

The type of the electrolyte used determines the characteristics of SCs. It largely determines the internal resistance, and the operating voltage cannot exceed the potential of the solvent's decomposition. Therefore, systems with an aqueous solution of an electrolyte have a low internal resistance, but the operating voltage must not exceed 1.2 V (the potential of

the water decomposition without account for the overpotential).

The capacitance of an electrochemical capacitor (EC) or a capacitor with a double electric layer (DEL) is described by the classical formula for a plane capacitor:

$$C = \frac{\varepsilon S}{d}, \quad (1)$$

where C is the capacitance of the SC, ε is the dielectric permeability, S is the electrode's surface area, and d is the DEL thickness. The difference is that an electrochemical capacitor in the case of identical electrodes (a symmetrical capacitor) represents two serially connected capacitors, so that its total capacitance is described as

$$\frac{1}{C} = \frac{1}{C_1} + \frac{1}{C_2}, \quad (2)$$

And, if $C_1 = C_2$, then

$$C = \frac{C_1}{2}. \quad (3)$$

According to formula (1), an increase in the specific electrode's surface area leads to an increase in the specific capacitance. Therefore, developers of SCs pay much attention to the selection of the active electrode material [2]. One can list the following main criteria for the active electrode material:

—it must be “ideally polarizable” in the range of potentials limited by the potentials of the electrochemical solvent's decomposition;

—it must have a large active material surface area to obtain large specific capacitance;

—it must have a high electron conductivity component to provide high power density of the electrochemical capacitors;

—it must be indifferent to the solution of the electrolyte.

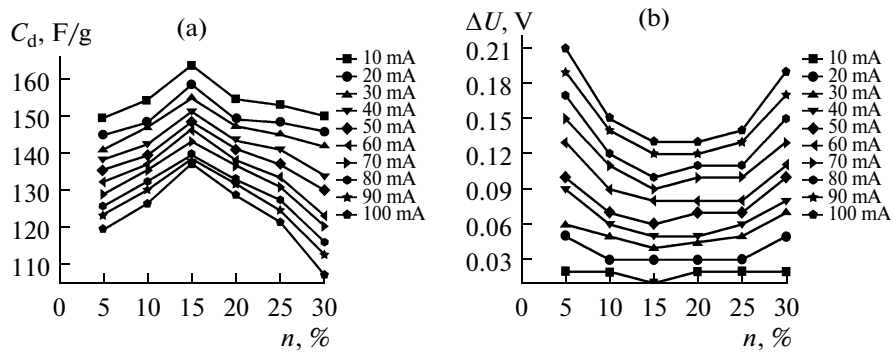


Fig. 1. Dependence of (a) the specific capacitance and (b) the internal resistance on the TEG percentage.

These criteria are best met by nanoporous carbon material (NCM); however, it has a low specific electric conductivity. Nanocomposite material (NComM) was developed to overcome this problem. The components of such a material are activated carbon with a highly developed surface ($>1000 \text{ m}^2/\text{g}$) and modified thermally exfoliated graphite (TEG) with resistance of about $2 \times 10^{-5} \text{ Ohm m}$ at a density of 0.5 g/cm^3 [3].

The aim of this work was to establish the dependence of the electrochemical parameters of the SC based on a mixture of nanoporous carbon and thermally exfoliated graphite on the concentration of the components of the above mixture.

MATERIALS AND RESEARCH TECHNIQUES

The nanocomposite material that was studied in this paper was made of nanoporous carbon and thermally exfoliated graphite. The nanoporous carbon was obtained from vegetable raw materials using the method of their hydrothermal carbonization at a water vapor pressure of $(12\text{--}15) \times 10^5 \text{ Pa}$ with further thermal activation at a temperature of $673 \pm 3 \text{ K}$. The TEG was obtained by the thermal decomposition of electrochemically oxidized graphite. The electrolyte was a 30% KOH aqueous solution.

The composite material (CM) was used to form electrodes in nickel gauze in the form of lamels, after which they were compacted at a pressure of 5 MPa. Two identical electrodes were separated by a separator of asbestos paper, a solution of electrolyte was poured over, and then they were sealed in a case.

The method of voltammetry at the sweep rates of 1 to 100 mV/s was used to study the dependence of the specific capacitance on the rate of the DEL charge–discharge. The rate of the variation of the electrochemical capacitor voltage is

$$s = \pm \frac{dU}{dt}, \quad (4)$$

then, the corresponding capacitor current is related to the capacitance through the equation $I = CdU/dt$ or

$I = Cs$. The specific capacitance of the NCM was calculated according to the formula

$$C_{\text{NCM}} = \frac{2I}{sm}, \quad (5)$$

where I is the current of the anodic or cathodic voltammogram branch, and m is the active electrode's mass. The specific capacitance of the carbon material as dependent on the discharge current in the range of 1 to 100 mA was calculated using the galvanostatic method. The specific capacitance of the ECs was calculated according to the formula

$$C_{\text{NCM}} = \frac{I_d t_d}{(U - \Delta U)m}, \quad (6)$$

where I_d is the discharge current, t_d is the discharge time, $U - \Delta U$ is the difference between the potentials at the limiting points of the discharge curve, and m is the NCM mass.

The internal resistance was determined on the basis of the potential's drop after ten charging–discharge cycles:

$$\Delta U = 2I_d R. \quad (7)$$

The potentiodynamic curves and the volt–faradic characteristics of the supercapacitors were studied using an AUTOLAB PGSTAT100 potentiostat. In addition, the dependences were studied of their specific capacitance and internal resistance on the concentration ratio of NCM : TEG on the basis of which they were formed. Activated carbon obtained from apricot kernels was used in the studies.

EXPERIMENTAL RESULTS AND DISCUSSION

The specific capacitance of SCs based on NCM–TEG nanocomposite materials with different contents of thermally exfoliated graphite is shown in Fig. 1a. With an increase in the TEG content from 5 to 15%, an increase in their specific capacitance from 150 to 164 F/g is observed (the scanning current is 10 mA). This is related to an increase in the NComM conduc-

Comparison of Early Stages of Copper Corrosion in Sulfate, Chloride, Humic and Soil Media¹

N. Souissi

Tunis El Manar University, Institut Préparatoire aux Etudes d'Ingénieurs,
El Manar-B.P.244 El Manar II-2092 Tunis, Tunisia

e-mail: nebilsouissi@gmail.com

Received March 11, 2012

Abstract—Early stages of copper corrosion behavior in NaCl, Na₂SO₄, humic acid and Tunisian soil have been examined using surface analysis (OM and AFM) as well as polarization curves. For different media, ranking has been established using R_q , E_{corr} , β_a , β_c , I_{corr} , B , R_p and E_b . The results reveal that patina formed at the Cu/Tunisian soil interface is the most protective covering.

DOI: 10.3103/S1068375513010134

INTRODUCTION

Understanding copper-based alloys corrosion behavior in soil is a great challenge. This is important not only to secure lifetime and reliability of containers used for underground nuclear waste storage, but also to provide valuable inputs concerning the mechanisms of alterations in cultural heritage artifacts.

Numerous studies have been conducted to understand copper-based alloys corrosion in soil environments [1–5]. However, to the best of our knowledge, the contribution of each single soil fraction (humic and inorganic) has not been exhaustively investigated so far. The present work is an attempt to compare the early stages of copper corrosion behavior in the Tunisian soil with those exhibited in chloride, sulfate, and humic electrolytes.

EXPERIMENTAL

Corrosion tests were conducted at room temperature in aerated solutions prepared from analytical grade reagents. Aqueous sulfate and chloride solutions (0.1 molL⁻¹) were used to simulate burying media. Humic acid (20 gL⁻¹) was also investigated as a corrosive electrolyte. Soil environments were obtained by mixing soil with distilled water until the concentration of 1 kgL⁻¹ was achieved. Soil composition was reported in previous works [6].

In the present investigation pure copper (99.999%) was used. The specimens were dried and hand-polished with emery paper up to the grade of 2500, then degreased with acetone, rubbed with cotton wool soaked in ethanol, dried at room temperature and immersed immediately into different media. After a four-hour immersion, the specimens were analyzed,

without further treatments, under transmitting light, using a polarizing Nikon ECLIPSE ME 600 microscope equipped with a digital camera. The atomic force microscopy (AFM) was performed in air with a Nanoscope IIIa Digital Instruments microscope equipped with an optical deflection system in combination with silicon cantilevers and tips working in tapping mode.

Electrochemical experiments were conducted at room temperature. A classical three-electrode cell was used with a saturated calomel electrode as reference and a platinum wire as a counter electrode. The electrochemical set-up consisted of an autoLab PGSTAT 30 potentiostat (Netherland). The Software GPES was used for voltammetric investigations and the scan rate was fixed at 10 mV s⁻¹. All experiments were replicated minimum three times.

RESULTS AND DISCUSSION

Effect of the Electrolyte Nature on the Electrochemical Interface Response

After four hours of immersion, the interfaces copper-electrolytes were submitted to linear polarization in the overpotential range of 1 V to 0.1 V. The scan rate was fixed at 10 mV s⁻¹. Such polarization speed is comparable with that used in previous works [6 and references therein]. The polarization curves are given in Fig. 1.

Irrespective of the electrolyte, four sections were evidenced on the polarization curves. The first (I) one, corresponding to the cathodic region, reflects the overpotential domain where the reduction reaction takes place. The second (II) is generally attributed to the plateau of oxygen diffusion. An “apparent Tafel” behavior was detected in the third interval. Mixed charge transfer and mass transport are usually assumed to control the reaction kinetics. Finally, the fourth

¹ The article is published in the original.

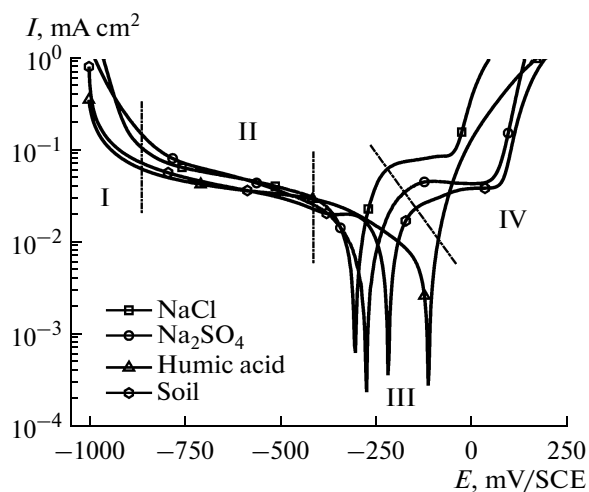


Fig. 1. Polarization curves of copper surfaces obtained after four hour immersion in various electrolytes. The potential was swept from -1 V to 0.25 V at a scan rate 10 mV s^{-1} .

overpotential interval corresponds to the anodic domain.

Extrapolation of the linear line to the corrosion potential gives a straight line, the slope gives both β_a ,

β_c , and the intercept gives the corrosion current. We also calculated the linear polarization resistance (R_p) by means of the Stern–Geary relationship:

$$R_p = \frac{\beta_a \beta_c}{2.3(\beta_a + \beta_c) I_{\text{corr}}} = \frac{B}{I_{\text{corr}}} \quad (1)$$

In Fig. 2, we present E_{corr} (a), β_a (b), β_c (c), I_{corr} (d), B (e), and R_p (f) evolutions for various environments.

After four hours of immersion in the humic medium, copper corrosion potential was the most anodic as it tended towards -0.111 V/SCE. Cathodic values for E_{corr} were measured for the material when submitted into inorganic media: -301 mV/SCE and -272 mV/SCE, chloride and sulfate, respectively. The intermediate value of E_{corr} , about -0.216 V/SCE, was delivered by copper when buried in the Tunisian soil, (Fig. 1a).

The apparent anodic Tafel slope was found to be close to 0.06 V^{-1} for the humic electrolyte (Fig. 2b). This value is equal to that generally observed for a pure material freshly immersed in aerated aqueous chloride electrolytes [7]. In spite of the existence of some patina layer at the surface, the rate of the copper anodic dissolution in humic medium, close to the corrosion potential, was under the influence of both charge transfer and mass transport.

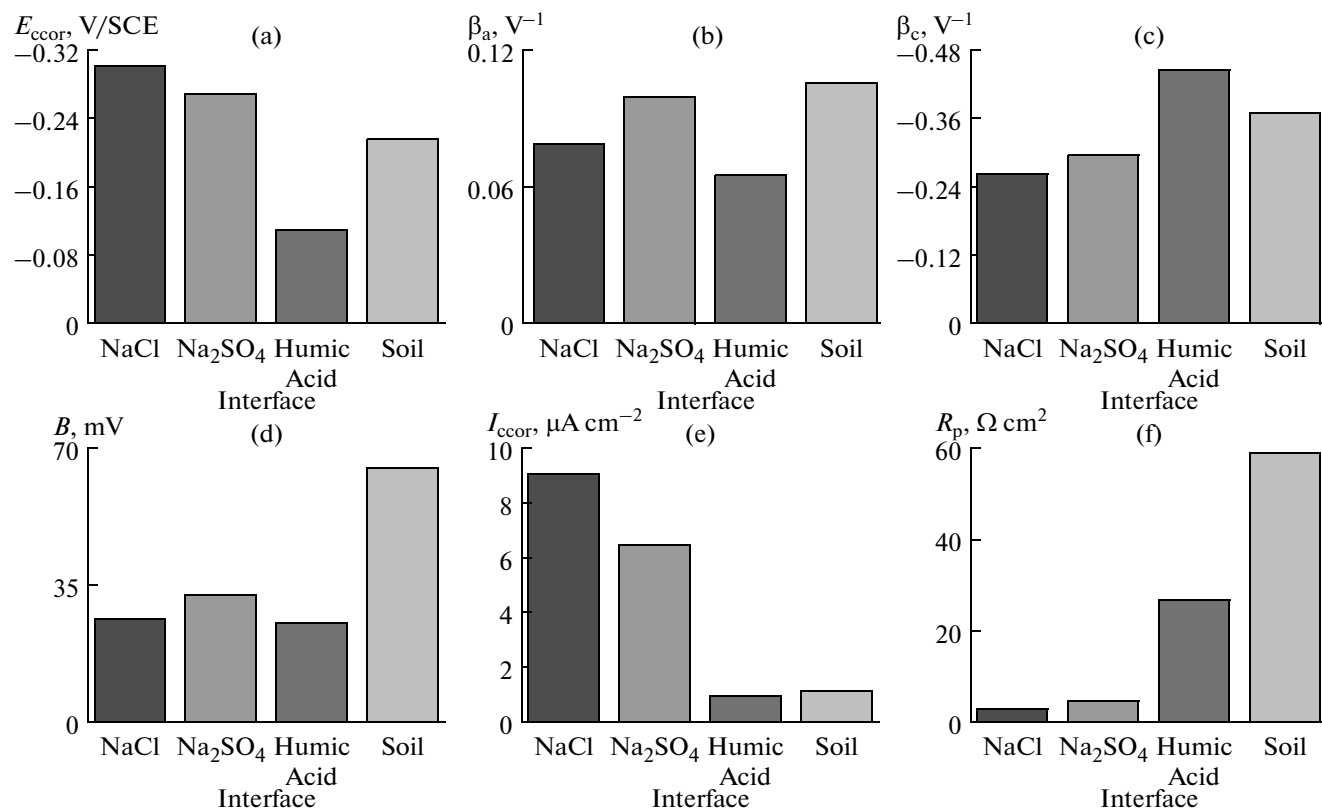


Fig. 2. Evolution of electrochemical parameters E_{corr} (a), β_a (b), β_c (c), B (d), I_{corr} (e) and R_p (f) for copper immersed in various environments.

Theoretical Analysis of Silicon Surface Roughness Induced by Plasma Etching¹

R. K. Tyagi

Department of Mechanical Engineering, Amity School of Engineering and Technology,
Amity University Uttar Pradesh, Noida, India

e-mail: tyagi_rk1@rediffmail.com

Received March 19, 2012; in final form, June 14, 2012

Abstract—A theoretical study of single-crystal silicon surface roughness induced by SF₆ plasma has been carried out by means of atomic force microscopy. Plasma which contains the velocity shear instability has been used to study the relation between the plasma parameters and subsequent surface roughness. The surface roughness has been examined in the dependence on experimental parameters. The results obtained by theoretical calculations are identical to the experimental ones. The present paper has quantified the influence of a DC electric field values on plasma parameters such as the ratio of ion flux to the neutral reactant flux (J^+/J_F), exposure time, DC electric field, magnetic field and inhomogeneity. Theoretical investigation shows that the roughness of silicon surface increases with the increase of the values of J^+/J_F , exposure time, of magnetic field, of inhomogeneity in a DC electric field and decreases through increasing the value of a DC electric field.

DOI: 10.3103/S1068375513010158

INTRODUCTION

The understanding of the contact mechanism between surfaces is important for the study of both electrical and mechanical properties of bonded interfaces. Such mechanical and electrical properties include the true contact area, bond strength, contact resistance, i.e. conductivity and reliability. Surface roughness plays a crucial role in the contact and friction of surfaces. In order to describe the roughness of a surface, statistical parameters for the distribution function of the roughness height such as the root mean square (*rms*) height, slope and radius curvature of asperity, have been used in several works. Those parameters can be directly related to the density of asperity, forms of asperity, and the standard deviation of the roughness height [1].

According to P. Verdonck [2], in general, plasma etching is a chemical etching, not a physical etching. This means that a chemical reaction takes place between a solid atom (from the film to be etched) and gas atoms to form a molecule, which is removed from the substrate. Because of the existing DC bias, there is always some sputtering, which is insignificant and in most cases should not be taken into account. Nevertheless, the importance of other physical aspects of the etching is emphasized in the studies of other authors [Verdonck, 2006, and Flamm 1986]. As is noted in [2], the main steps in the etching process commented in

more detail on the example of the etching of silicon using sulphur hexafluoride (SF₆) are:

- (i) Formation of the reactive particle;
- (ii) Arrival of the reactive particle at the surface to be etched;
- (iii) Adsorption of the reactive particle at the surface;
- (iv) Chemisorption of the reactive particle at the surface, i.e. a chemical bond is formed;
- (v) Formation of the product molecule;
- (vi) Desorption of the product molecule;
- (vii) Removal of the product molecule from the reactor.

For the similar idea regarding etching, see also [3].

As outlined in [4], the problem of interface roughness has received particular attention, especially the development of its theoretical base. This is due to its practical connection to the thin-film growth. However, rather little effort has been made so far to interpret experimental data in terms of kinetic roughening as can be done for the interaction of plasma with different materials. In this regard, it is worth noting here that an independent varying of plasma parameters is an advantage over conventional machining process. As a major result from [4], an empirical analytical form describing the surface roughness as a function of plasma parameters has been established.

As is known, for the integrated circuits with a decrease of their dimensions the roughness of compound material layers deposited on silicon at different

¹ The article is published in the original.

steps of a device fabrication becomes so critical that it needs to be carefully assessed before and after etching. Thereby, it is evident that at such tiny dimensions the plasma etching of the surface cannot be considered being uniform. Thus, it is necessary to take into account roughness, which is closely connected with such plasma parameters as ion energy, ion current density, and the flow of the reacting species. As indicated in [5], the investigated range of roughness values is not amenable to conventional surface metrology techniques such as the scanning electron microscopy (SEM), profilometry, etc. The transmission electron microscopy (TEM) is quite a cumbersome technique to be routinely used since sample preparation takes up too much time. Moreover, a nondestructive sample analysis is not possible by the latter technique. The scanning tunneling microscopy (STM) and atomic force microscopy (AFM) have now become the up-to-date tools to carry out such measurements. The AFM provides a unique opportunity to study the extent of the silicon roughness produced at the SF₆ plasma etched silicon surfaces [5].

The central goal of patterning by plasma processing is to obtain any high rate, while preserving anisotropy, uniformity, and selectivity at the obtained rate. Significant advances in fundamental understanding of plasma-assisted processes have been reported in the recent past, although engineering development of a new system continues to rely heavily upon trial and error procedures [6]. Using a one-dimensional radial dispersion model, the authors [6] examine the role of physical factors such as etchant convection and diffusion, which are determined by the concentration of the etchant, and also present a detailed study of the etch rate of a polymer in an oxygen plasma as a function of pressure, power, and flow rate.

Further, mathematical model by Tyagi et al [7, 8] for the plasma containing velocity shear instability is presented and it is considered that the surface roughness is formed by impacts of ions. To analyse the obtained results the phenomenological power law for the heights of surface roughness from [4] is used.

MATHEMATICAL MODEL AND PLASMA GENERATION WHICH CONTAINS VELOCITY SHEAR INSTABILITY

Plasma generated in laboratory conditions contains both positive K⁺ ions and negative SF₆⁻ ions. Potassium ions are produced by spraying potassium atoms onto a tungsten plate and SF₆⁻ ions are produced from the electrons released from another tungsten plate. The generation and control of the parallel velocity shear are achieved by individual biasing of each segment of the segmented ion source, i.e. a difference between voltages applied between two con-

ductive segments. The generation of a parallel velocity shear instability can be achieved with an electrostatic energy analyzer and through the laser-induced fluorescence diagnostic technique. Negative ions are produced by introducing SF₆ gas into the potassium plasma. An SF₆ molecule has a great electron attachment cross-section for the electron energies less than 1 eV. This is why both negative and positive ions are formed in different layers, that have shear of velocity and density gradient in a respective layer. The detailed description of generation of velocity shear instability is described by the author of the present paper and his colleagues in [8, 10].

Since ions are electrical charges, their trajectories and velocities are influenced by electric and magnetic fields. Using our earlier results [8], it is easy to obtain the expression for the group velocity of an electrostatic ion-cyclotron wave by assuming small perturbations of the electric field E_1 , magnetic field B_1 , and distribution function f_{s1} . For the perturbed values of the electric and magnetic fields the harmonic dependences as $\exp(i(kr - \omega t))$ are assumed. Considering the ion velocity v to be equal to the group velocity of the wave, i.e. to $\partial\omega/\partial k$, and using the expression for the real frequency ω , of the wave incident on the workpiece surface, Eq. (15) from our earlier work [8] can be written as:

$$\frac{\bar{\omega}'}{\Omega_i} = -\frac{b_1}{2a_1} \left[1 \pm \sqrt{\left(1 - \frac{4a_1 c_1}{b_1^2}\right)} \right] \quad (1)$$

where:

$$a_2 = a_2 \left(\frac{\Omega_i}{k_{\parallel} \alpha_{\parallel i}} \right)^2, \quad b_1 = \frac{\Omega_i}{k_{\parallel} \alpha_{\parallel i}} b_2 - \frac{2k_{\perp} \Delta'}{k_{\parallel}^2 \alpha_{\parallel i}^2} a_2 \Omega_i,$$

$$a_2 = \frac{\eta_e T_{\perp i}}{\eta_i T_{\parallel i}} + \frac{T_{\perp i}}{T_{\parallel i}} - \Gamma_n(\mu_i) \frac{T_{\perp i}}{T_{\parallel i}},$$

$$b_2 = \frac{\Gamma_n(\mu_i) k_{\perp}}{2k_{\parallel}} \varepsilon_n \rho_i \frac{\alpha_{\perp i}}{\alpha_{\parallel i}} - \frac{\Gamma_n(\mu_i) k_{\perp}}{2k_{\parallel}} - \frac{\Gamma_n(\mu_i) k_{\perp} n \Omega_i}{2k_{\parallel}^2 \alpha_{\parallel i}},$$

$$c_1 = \frac{\Gamma_n(\mu_i) T_{\perp i}}{2T_{\parallel i}} \left(1 - \frac{k_{\perp}}{k_{\parallel}} A_i \right) - \frac{b_2 k_{\perp} \Delta'}{k_{\parallel} \alpha_{\parallel i}} + \frac{k_{\perp}^2 \Delta'^2}{2k_{\parallel}^2 \alpha_{\parallel i}^2},$$

$$\eta_i = 1 - \frac{\bar{E}'_i(x)}{4\Omega_i^2}, \quad \eta_e = 1 - \frac{\bar{E}'_e(x)}{4\Omega_e^2}, \quad \bar{\omega}' = \bar{\omega} - n\Omega_i,$$

$$E(x) = E_0 \left(1 - \frac{x^2}{a^2} \right), \quad \bar{E}(x) = \frac{e_s E(x)}{m_s},$$

$$\Omega_s = \frac{e_s B_0}{m_s}, \quad \alpha_{\perp s} = \left(\frac{2k_B T_{\perp s}}{m_s} \right)^{1/2}, \quad \alpha_{\parallel s} = \left(\frac{2k_B T_{\parallel s}}{m_s} \right)^{1/2},$$

$$\xi = \frac{\bar{\omega} - (n+p)\Omega_s - k_{\perp} \Delta'}{k_{\parallel} \alpha_{\parallel s}}, \quad \Delta' = \frac{\partial \Delta}{\partial t},$$

Photoelectrochemical Properties of Oxide Films Formed by Anode Plasma Electrolytic Oxidation on Titanium in Water Solutions¹

E. P. Grishina^a, N. O. Kudryakova^a, P. A. Rumyantsev^a, A. V. Zhironov^b, Yu. P. Gladiy^c, and P. N. Belkin^b

^a*G.A. Krestov Institute of Solutions Chemistry of RAS, Academicheskaya St. 1, Ivanovo, 153045 Russia*

^b*N.A. Nekrasov Kostroma State University, 1 May St. 14, Kostroma, 156961 Russia*

^c*Kostroma State Technological University, Dzerzhinsky St. 17, Kostroma, 156005 Russia*

e-mail: epg@isc-ras.ru, belkinp@yandex.ru, timber72gr@mail.ru

Received June 27, 2012; in final form, September 4, 2012

Abstract—It is shown that films of titanium dioxide obtained by anodic plasma electrolytic processing of commercial titanium in an aqueous solution of ammonium chloride are photosensitive. Incident photon to charge carrier efficiency (IPCE) in the near ultraviolet (366 nm) reached 8.5%. Magnitude of the photocurrent generated by the films obtained under optimum processing conditions decreases no more than 20% at the transition from the ultraviolet to the mixed light.

DOI: 10.3103/S1068375512060026

INTRODUCTION

Titanium dioxide is perhaps the most intensively studied materials among semiconductor oxide materials which are used in photoelectrochemical cells. TiO₂ exhibits high catalytic activity in the electrochemical reactions in converters of solar energy and has excellent corrosion resistance in electrolyte solutions.

There are various methods of photosensitive film TiO₂-electrodes producing with n-type conductivity: sputtering, hydrothermal and sol-gel deposition of oxide anode methods and thermally oxidation of titanium, etc. [1–5]. Both a thermal oxidation of titanium in oxygen or air at temperatures above 400°C and anodic oxidizing titanium in aqueous and non-aqueous electrolyte solutions are considered to be most simple and manageable processes [1]. Anode plasma electrolytic oxidation of titanium is characterized by simultaneous actions of high temperature and anodic polarization [6]. Specificity of this method is the formation of a vapor-gas envelope around anode if the anode area is much smaller than the cathode area. Energy of power supply is released in the vapor-gas envelope then the metal anode is heated to temperatures of 400–1000°C, and an electrochemical reactions occur in the system of the electrolyte—envelope—anode. Electrochemical system may contain a four phases due to formation of the oxide layer on the metal surface. This case takes place at the oxide coatings on aluminium alloys [7]. Oxide layer does not play a significant role in some applications. There are, however, processes where the oxide layer significantly

improves the corrosion properties of steel depending on the voltage and heating temperature, electrolyte composition, etc. [8]. Anode saturation with nitrogen and oxygen can reduce the corrosion rate of commercial titanium by two orders for continuous trials and by factor 8 in the cyclic tests in a solution containing 6% hydrochloric acid with the addition of protein-vitamin concentrate (20%) [9]. Similar results have been obtained for other titanium alloys [10].

Consequently, it can be assumed that the treatment combining thermal-mechanical and electrochemical effects leads to the formation on the titanium electrode the photo-sensitive oxide layer.

The aim of this work is to study the influence of plasma electrolytic conditions on the photoelectrochemical properties of the formed surface films.

EXPERIMENTAL APPARATUS AND METHODS

Features of the anode plasma electrolytic heating of the titanium studied on cylindrical samples of 8 mm diameter and 15 mm length. The sample temperature is measured with the use of a digital multimeter APPA 109N (mean precision ±0.5%) in the registering mode with a thermocouple that was inserted into the sample approximately 1 mm to the low surface by drilling a hole.

Photoelectrochemical properties of oxidized commercial titanium VT1-0 was studied on samples of rectangular shape (50 × 8 × 1.5 mm). All the samples were ground by grit paper to their clarification and cleaned by ethyl alcohol before plasma heating.

¹ The article was translated by the authors.

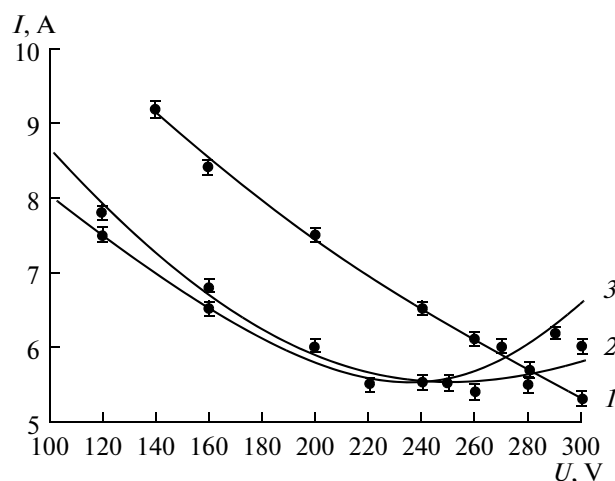


Fig. 1. The current-voltage characteristics of the anode heating of the titanium samples in an aqueous solution of ammonium chloride. Concentration of NH_4Cl (wt %): 1—5; 2—10; 3—15.

Plasma electrolytic treatment of titanium was carried out in 2 M aqueous solution of nitrate, chloride or ammonium sulfate. Oxidation of vertical oriented and positive polarized samples was carried out by its dipping into the work chamber at a rate of 1.5 mm/s. Electrolyte circulation was realized by pump at rates of 5 L/min, the volume flow rate was measured by a flowmeter RMF-0.16 GUZ (accuracy to within (2.5%). Cooling water is circulated through the heat exchanger. The electrolyte temperature at the inlet to the working chamber was maintained at $(28 \pm 2)^\circ\text{C}$. After the treatment the samples was lifted from the electrolyte, and then the voltage is switched off to avoid quenching with the exception of a noted cases.

Mass change of the sample during oxidation was determined by gravimetric method using an analytical balance VLR-200 (weighing accuracy 10^{-4} g). Titanium content passed into the solution was determined (based on TiO_2) by gravimetric method. Electrolyte with titanium compounds was boiled to remove ammonium ions and chlorine; residue was filtered off and washed with water, ignited and weighed. Phase composition of the surface layer on the treated samples was determined by X-ray diffraction (DRON-4) with $\text{Cu } K_\alpha$ radiation. Surface of the treated samples was observed using an optical microscope “Mikromed” with attached WEB-camera “DCM-130” (increasing $\times 40$).

Photoelectrochemical properties of oxidized titanium electrodes were studied at a temperature of 18°C in a quartz cell (92–95% light transmission). The samples were illuminated by monochromatic ultraviolet light (254 or 366 nm) from the source Benda UV-Handlampe NU-6 W or mixed light from the gas-discharge lamps of high pressure HWL (MBFT) 160 W. Intensity of light falling from the source Benda UV-Handlampe NU-6 W is recorded by monochromator of the spectrometer AvaSpec-3648 with diffrac-

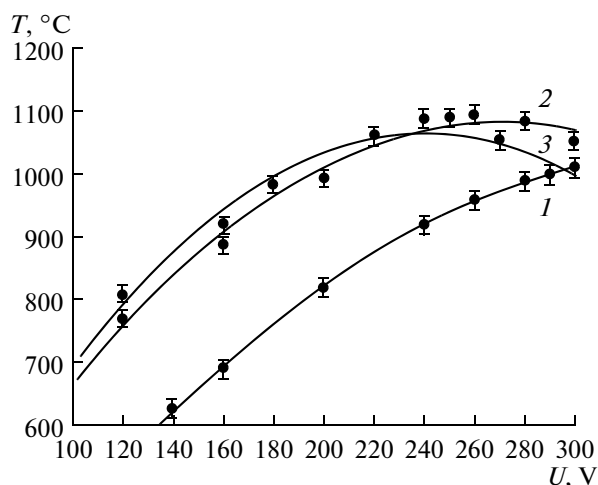


Fig. 2. The current-temperature characteristics of titanium samples heating in an aqueous solution of ammonium chloride. Concentration of NH_4Cl (%): 1—5; 2—10; 3—15.

tion grating 1200 lines/mm, the width of the entrance slit was 10 μm . Real resolution of the instrument was ~ 0.17 nm in the wavelength range 250–350 nm.

Titanium electrode photopotential E_{ph} (the potential difference in light and in the dark [11]) was fixed with respect to the shaded platinum electrode using a measuring system of potentiostat PI50-1 (measurement error ± 5 mV). Photocurrent was measured under conditions imitating an operation of photovoltaic cells. A short-circuited electrochemical $\text{Ti} | \text{oxide} | 0.5 \text{ M } \text{Na}_2\text{SO}_4 | \text{Pt}$ cell and also circuit with resistor set connected in series including self-recording ampere-voltmeter (measuring range 10 μA , measurement error 1.5%) was used. The distance between the electrodes was 4 mm. Polarization potential of oxidized titanium was measured relatively to a saturated silver-chloride electrode.

RESULTS

Anode Heating Specificity of Commercial Titanium

Anode heating stipulation is the formation of the continuous and stable vapor-gas envelope surrounding sample. This state is reached in the range of 80–300 V. Kind of current-voltage and temperature-voltage characteristics of the titanium heating is analogues to ones received during the anodic steel heating. Specificity heating titanium consists in a presence of increasing current branches at voltages above 240–250 V (Figs. 1 and 2). Current-voltage characteristics of heating steels are usually monotonically decreasing. This fact is explained by the expansion of vapor-gas envelope with the voltage growth and a corresponding increase in its electric resistance. There is also a certain shift of the maximum temperature of the titanium samples in the region of lower voltages with increasing concentration of the electrolyte.